Characteristics of Long-Duration Heavy Precipitation Events along the West Coast of the United States

Benjamin J. Moore,[a] Allen B. White,[a] and Daniel J. Gottas[a]

[a] NOAA/Physical Sciences Laboratory, Boulder, Colorado

ABSTRACT: Prolonged periods (e.g., several days or more) of heavy precipitation can result in sustained high-impact flooding. Herein, an investigation of long-duration heavy precipitation events (HPEs), defined as periods comprising ≥3 days with precipitation exceeding the climatological 95th percentile, is conducted for 1979–2019 for the U.S. West Coast, specifically Northern California. An objective flow-based categorization method is applied to identify principal large-scale flow patterns for the events. Four categories are identified and examined through composite analyses and case studies. Two of the categories are characterized by a strong zonal jet stream over the eastern North Pacific, while the other two are characterized by atmospheric blocking over the central North Pacific and the Bering Sea–Alaska region, respectively. The composites and case studies demonstrate that the flow patterns for the HPEs tend to remain in place for several days, maintaining strong baroclinicity and promoting occurrences of multiple cyclones in rapid succession near the West Coast. The successive cyclones result in persistent water vapor flux and forcing for ascent over Northern California, sustaining heavy precipitation. For the zonal jet patterns, cyclones affecting the West Coast tend to occur in the poleward jet exit region in association with cyclonic Rossby wave breaking. For the blocking patterns, cyclones tend to occur in association with anticyclonic Rossby wave breaking on the downstream flank of the block. For Bering Sea–Alaska blocking cases, cyclones can move into this region in conjunction with cyclonically breaking waves that extend into the eastern North Pacific from the upstream flank of the block.

SIGNIFICANCE STATEMENT: We sought to understand atmospheric processes that result in heavy precipitation events along the U.S. West Coast that span long durations (≥3 days) and thus pose significant flooding threats. We analyzed events over Northern California and identified four distinct flow patterns over the North Pacific that support their occurrence: two exhibiting a strong west–east jet stream and two exhibiting a wavy "blocked" jet stream. These patterns tend to persist for several days and promote the landfall of multiple extratropical cyclones in rapid succession along the West Coast, thereby maintaining the ingredients for precipitation over Northern California for extended periods (5–6 days). The physical understanding established by our results could have utility for forecasting heavy precipitation.

KEYWORDS: Blocking; Dynamics; Extratropical cyclones; Extreme events; Precipitation; Rossby waves

1. Introduction

Prolonged periods of quasi-continuous and often heavy precipitation, spanning several days to beyond a week, can result in extreme precipitation accumulations and sustained high-impact flooding. Noteworthy examples of this class of event, hereafter referred to as a long-duration heavy precipitation event (HPE), occurred in July 2010 in Pakistan (Martius et al. 2013); June 2013 in central Europe (Grams et al. 2014); September 2013 in the Colorado Front Range (Gochis et al. 2015); February 2017 in Northern California (White et al. 2019); and August 2017 in Houston, Texas, due to Hurricane Harvey (Risser and Wehner 2017). Flooding associated with these events can have a variety of adverse impacts, including fatalities, economic disruption, and costly damage to crops, property, and infrastructure. In addition, these events can sometimes make beneficial contributions to water resources (e.g., White et al. 2019). Given the potential impacts of long-duration HPEs, there is a need for improved understanding of the dynamical processes governing these events.

At midlatitudes, heavy precipitation tends to be produced by transient weather systems, such as extratropical cyclones (e.g., Pfahl and Wernli 2012). These systems are usually mobile (e.g., Wallace et al. 1988); hence, from an Eulerian perspective, the associated regions of precipitation tend to be short lived (e.g., <1 day). There are, however, two pathways through which the duration of precipitation at a location may be substantially lengthened: 1) a system stalls and becomes quasi-stationary for an extended period, and 2) multiple systems pass over the location in rapid succession. The first pathway can emerge when the movement of a system is impeded (e.g., Lenggenhager et al. 2019), or when a system moves into an environment of weak background flow, as can occur for cutoff extratropical cyclones (e.g., Doswell et al. 1998) and some tropical cyclones (e.g., Kossin 2018). The second pathway can emerge through repeated passage of, for example, cyclones (e.g., Priestley et al. 2017a) or mesoscale convective systems (e.g., Tuttle and Davis 2006) through a geographically fixed corridor over a period of several days. In these situations, systems serially cluster such that they occur at a location much more frequently than is expected due to chance.

Findings of prior case studies (e.g., Weaver 1962; Lackmann and Gyakum 1999; Sodemann and Stohl 2013; Grams et al. 2014; Priestley et al. 2017a; Moore et al. 2020) suggest that serial clustering of extratropical cyclones is a principal process resulting in long-duration HPEs at midlatitudes. This process, consistent with the concept of "cyclone families" (Bjerknes and Solberg 1922),

occurs when multiple cyclones develop and follow a similar path in rapid succession (separated by intervals of, e.g., ~1–2 days). The aforementioned case studies collectively indicate that heavy precipitation can be sustained for several days or more by forcing for ascent and water vapor supply linked to clustered cyclones.

Water vapor fluxes associated with extratropical cyclones are often concentrated within atmospheric rivers (e.g., Newell et al. 1992; Zhu and Newell 1998; Ralph et al. 2004, 2018) aligned with the low-level jet in the warm sector. Prolonged heavy precipitation is favored when an atmospheric river stalls (e.g., Ralph et al. 2019) or when cyclones cluster such that successive atmospheric rivers affect the same region (Fish et al. 2019). In mountainous regions, such as those along the U.S. West Coast, precipitation can be geographically anchored by orographic forcing as persistent water vapor flux impinges on elevated terrain (e.g., Ralph et al. 2013; Neiman et al. 2016).

Cyclone clustering may result from the development of secondary or frontal-wave cyclones along a cold front that trails an antecedent cyclone (e.g., Priestley et al. 2020). These cyclones can reinforce and extend the duration of an atmospheric river linked to an antecedent cyclone (e.g., Ralph et al. 2011; Neiman et al. 2016). Secondary cyclogenesis often results from frontal instability (e.g., Schär and Davies 1990; Joly and Thorpe 1990; Schemm and Sprenger 2015) and may involve other mechanisms, such as latent heating (e.g., Weijenborg and Spengler 2020) and frontal strain effects (Dacre and Gray 2006).

Long-lived (e.g., from several days to two weeks) patterns of the large-scale (i.e., from synoptic- to planetary-scale) flow can modulate extratropical jet streams and concomitant baroclinic storm tracks (e.g., Rex 1950; Reinhold and Pierrehumbert 1982; Dole 1986; Lau 1988; Nakamura and Wallace 1990; Athanasiadis et al. 2010; Madonna et al. 2017), and therefore can significantly influence regional precipitation distributions (e.g., Mo and Higgins 1998; Robertson and Ghil 1999; Lavers and Villarini 2013; Pasquier et al. 2019). The persistence of these patterns beyond the time scale of individual synoptic-scale disturbances can occasionally foster cyclone clustering (Mailier et al. 2006). Clustering can occur in patterns featuring a quasi-stationary and zonally extended upper-level jet stream (e.g., Pinto et al. 2014; Priestley et al. 2017b). The jet acts as a persistent waveguide (e.g., Martius et al. 2010) for synoptic-scale Rossby waves, which may repeatedly induce baroclinic instability and cyclogenesis. Clustered cyclone activity in these patterns tends to occur in the jet exit region and may coincide with cyclonic and anticyclonic wave breaking on the poleward and equatorward sides of the jet, respectively (Priestley et al. 2017b).[1]

---

[1] Rossby wave breaking is defined as a rapid and irreversible deformation of material [i.e., potential vorticity (PV) on an isentropic surface] contours (McIntyre and Palmer 1983). On synoptic scales, wave breaking typically occurs in the latter stages of baroclinic wave life cycles under the influence of background meridional shear (Thorncroft et al. 1993). Waves can break cyclonically or anticyclonically based on the direction of overturning of PV contours.

Cyclone clustering and long-duration HPEs can also occur in patterns characterized by atmospheric blocking (e.g., Grams et al. 2014; Moore et al. 2020). In these patterns, successive episodes of cyclogenesis and cyclonic wave breaking can occur on the upstream flank of a quasi-stationary blocking ridge or anticyclone. Here, the blocking ridge acts to impede and divert synoptic-scale waves, causing clustering in a manner analogous to a traffic jam (Mailier et al. 2006; Nakamura and Huang 2018). Eddy fluxes of heat and momentum tied to this clustering can be integral for the formation and maintenance of blocking (e.g., Shutts 1983; Mullen 1987; Nakamura et al. 1997). Stationary regions of blocking can force a recurrence of longitudinally aligned synoptic-scale Rossby waves downstream (Röthlisberger et al. 2019) that can result in protracted periods (e.g., 10–14 days) of precipitation (Barton et al. 2016). Rossby wave breaking linked to blocking can sometimes result in the formation of singular slow-moving troughs and cutoff cyclones that support long-duration HPEs (e.g., Lenggenhager et al. 2019). In cases of high-latitude blocking, a persistent jet stream and coaligned storm track is often established at midlatitudes equatorward of the blocked region (e.g., Nakamura and Wallace 1990; Carrera et al. 2004; Benedict et al. 2019). This configuration can foster clustering of cyclones and atmospheric rivers (Fish et al. 2019) leading to long-duration HPEs (Moore et al. 2020).

To date, research on flow patterns and dynamical processes associated with long-duration HPEs has been predominantly conducted through case studies. Systematic climatological studies on these aspects are currently lacking. Such studies are critical for gaining a comprehensive understanding of the processes governing these events. The current study addresses this research gap by conducting a 41-yr climatological investigation of long-duration HPEs. The primary objectives of this investigation are 1) to identify principal large-scale flow patterns linked to long-duration HPEs, and 2) to diagnose, through composite analyses and case studies, processes within those patterns that act to sustain heavy precipitation. To limit the scope of the study, we focus on events in the West Coast region of the United States. We hypothesize that this region is particularly susceptible to long-duration HPEs due to 1) its proximity to the terminus of the North Pacific storm track, a preferred region for cyclone clustering (Mailier et al. 2006), during the cool season, and 2) the preponderance of complex orography, which can act to anchor precipitation as cyclones and atmospheric rivers make landfall.

2. Data and methods

a. Climatology of long-duration heavy precipitation events

Gridded precipitation data from the NOAA Climate Prediction Center Unified Precipitation Dataset (UPD; Higgins et al. 2000; NOAA/NCEP/CPC 2020) were used to construct a climatology of long-duration HPEs for 1979–2019. This dataset is based on precipitation gauge observations and consists of daily (1200–1200 UTC) accumulations on a 0.25° grid covering the conterminous United States for 1948–present. The interpolation scheme used to generate

the UPD causes smoothing and attenuation of gauge totals and can misrepresent totals in regions where gauges are sparse (Chen et al. 2008; Ensor and Robeson 2008). Despite these issues, the UPD was used because it provides a continuous observation-based record that enables a robust climatological analysis.

We sought multiday periods that not only culminated in large precipitation accumulations but also comprised several successive days of heavy precipitation. To this end, heavy precipitation occurrences were first flagged in the daily time series at each grid point as an amount exceeding the climatological 95th percentile, computed for all days during 1979–2019 with amounts > 0 mm (Fig. 1a). Second, at each gridpoint sequences of heavy precipitation days separated by a gap of ≤1 day were identified. Third, sequences comprising ≥3 heavy precipitation days were selected and considered to indicate the occurrence of a long-duration event. Imposing longer minimum durations (e.g., 4 and 5 days) does not qualitatively affect the results but substantially reduces the number of events (not shown).

A map of the frequency of ≥3-day heavy precipitation sequences (Fig. 1b) demonstrates that long-duration events occur at nearly all grid points over the United States but with greatest frequency along the West Coast as well as in portions of the Rocky Mountains. The sequences along the West Coast predominantly occur in the extended winter, defined as November–March (Fig. 1c), the season during which the region experiences most of its precipitation and is most frequently impacted by extratropical cyclones. The results in Figs. 1b,c support our hypothesis that the West Coast is particularly susceptible to long-duration events and provide justification for focusing on this region. Especially high frequencies (e.g., event counts > 16; Figs. 1b,c) tend to be collocated with major mountain ranges (Fig. 2a), highlighting the influence of orographic forcing. Precipitation totals attributable to long-duration sequences (Fig. 2b) are maximized in Northern California along the Sierra Nevada and at the north end of the Central Valley, and in western Washington along the Olympic and Cascade mountains (see Fig. 2a). The sequences in these regions account for considerable fractions of the total accumulated precipitation (maximum values > 12%; Fig. 2b) and of daily heavy precipitation occurrences (maximum values > 28%; Fig. 2c) during 1979–2019.

To further limit the scope of this study, we focus only on events during the extended winter in the northern part of California (37°–42°N, 119.5°–124.5°W, referred to as the Northern California domain; Fig. 2a). This subregion was chosen because of the comparatively large precipitation contributions of long-duration events therein (Fig. 2b) and because we sought to add to the extensive body of research on precipitation and related weather systems for the region (e.g., Ralph et al. 2006; Dettinger et al. 2011; Cordeira et al. 2013, among many others). Days for which the precipitation at ≥10 grid points in the domain occurred as part of a long-duration (≥3 days) sequence were first identified (385 days). Qualifying days separated by ≤1 day were then merged, resulting in a final sample of 79 long-duration HPEs.
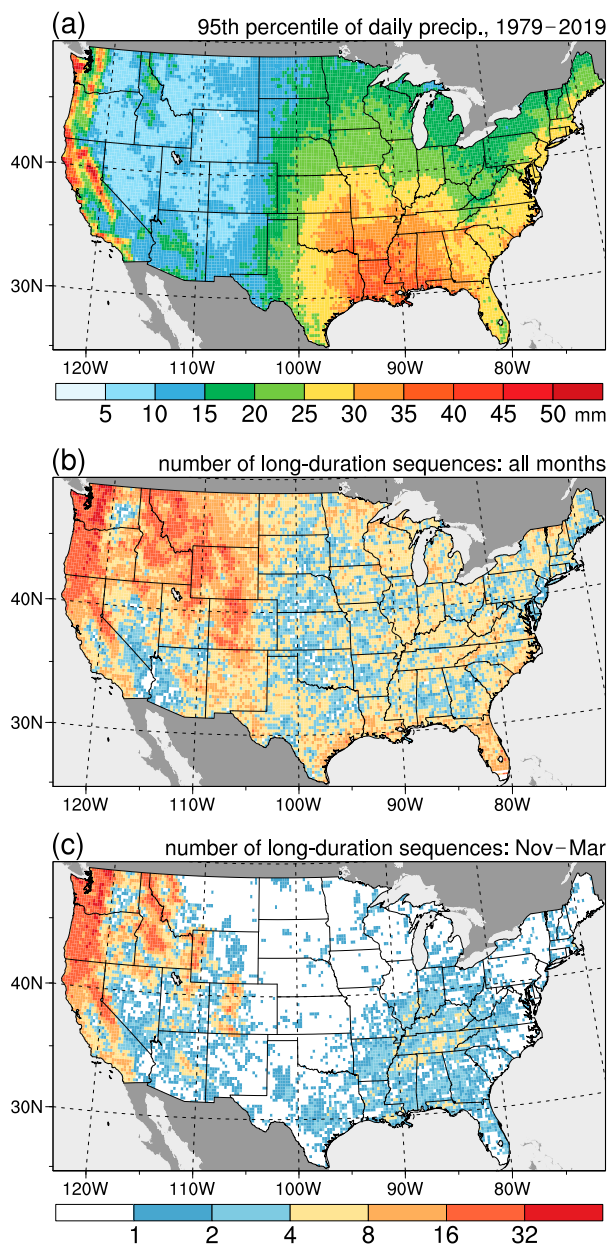

FIG. 1. (a) The 95th percentile of precipitation (mm; upper color bar) for all days during 1979–2019 with amounts > 0 mm. The number of long-duration heavy precipitation sequences (lower color bar) during 1979–2019 for (b) all months and (c) November–March.

Imposing less restrictive gridpoint count criteria increases the sample size (e.g., 141 events for a threshold of 1 point); likewise, imposing more restrictive criteria decreases the sample size (e.g., 44 events for a threshold of 30 points). The threshold of 10 points was chosen to filter out small-scale precipitation events while still maintaining a sufficiently large event sample. The onset and end days for the 79 events were defined as the earliest onset day and the latest end day, respectively, among all gridpoint sequences included in the
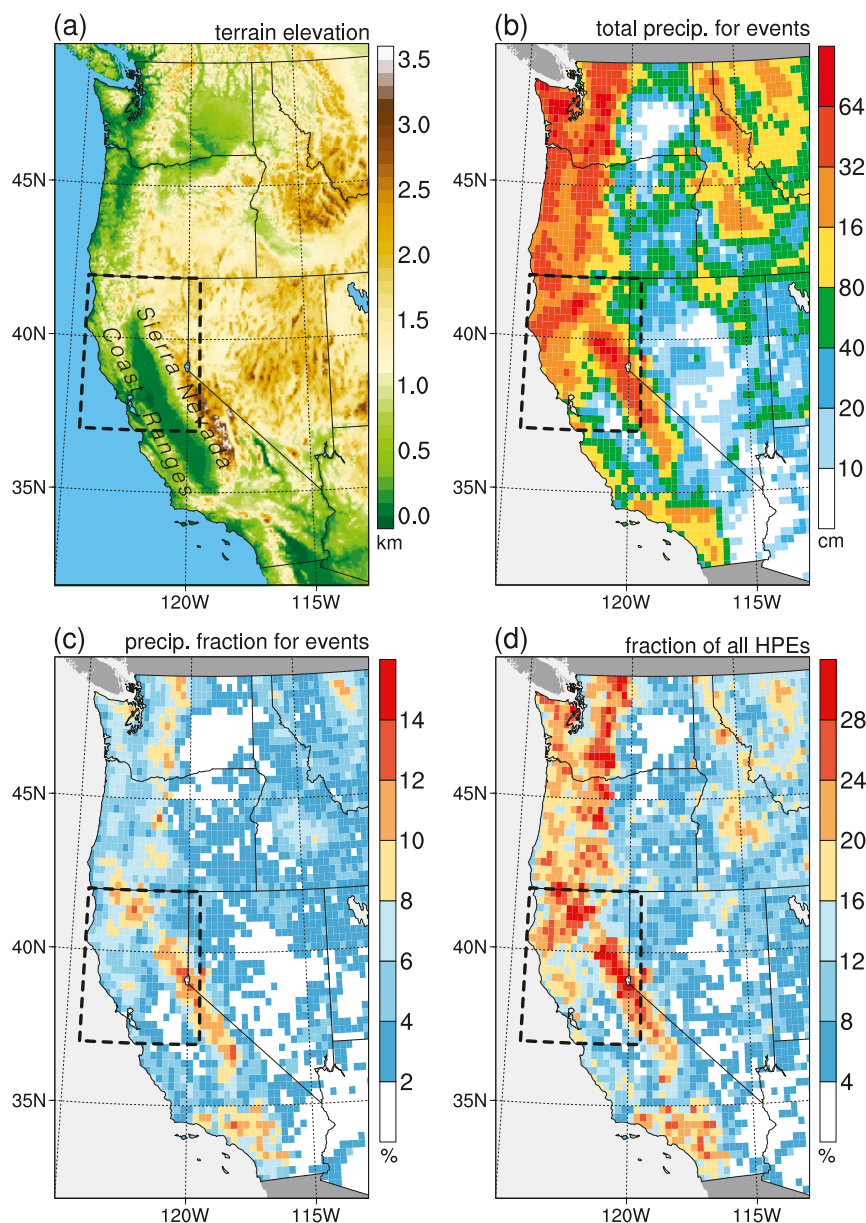
FIG. 2. (a) Terrain elevation ((km); major lakes and ocean masked in blue) from the 1-arc-min NOAA/NCEI ETOPO1 dataset (Amante and Eakins 2009; NOAA/NCEI 2020). (b) The total precipitation (cm) produced by long-duration heavy precipitation sequences during 1979–2019. (c) As in (b), but expressed as a percent of the total accumulated precipitation for 1979–2019. (d) The percent of daily heavy precipitation occurrences during 1979–2019 that were part of a long-duration sequence. The dashed black box denotes the Northern California domain from which long-duration HPEs were selected.

event. A reference time t_o was defined as 0000 UTC on the onset day.

b. Flow-based categorization of events

The long-duration HPEs were objectively categorized based on the large-scale atmospheric conditions under which they occurred using a method that combines empirical orthogonal function (EOF) analysis (Wilks 2011, his section 12.1) with

fuzzy c-means clustering [see Bezdek et al. (1984) for technical details]. The EOF analysis was performed on the 5-day mean 500-hPa geopotential height anomaly fields over the North Pacific and western North America (Figs. 3a,b) from t_o to $t_o +$ 120 h for the 79 HPEs. The 5-day averaging period was sufficient to distinguish persistent flow features, such as blocking, while filtering out more transient features. Clustering was performed in the phase space (Fig. 3c) defined by the two
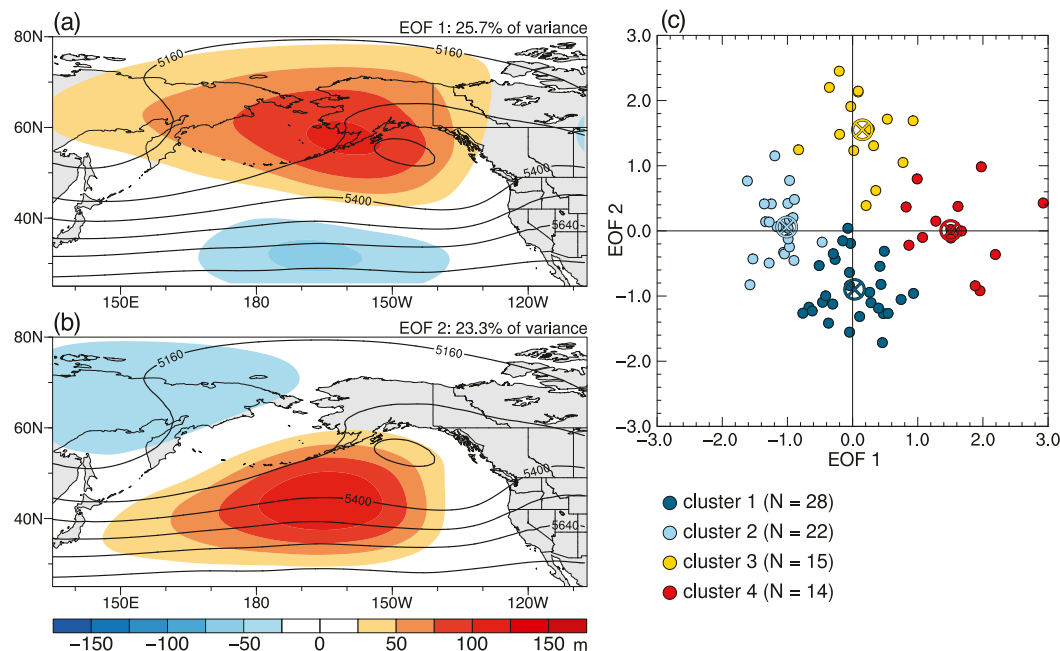
FIG. 3. The (a) first and (b) second EOFs (m; shading) of the 5-day mean 500-hPa geopotential height anomaly fields associated with the 79 long-duration HPEs overlaid by the mean geopotential height field (contours every 120 m) for all 79 events. (c) Scatterplot of the HPEs in the phase space for the first two EOFs. The projections onto the EOFs in (c) are normalized by the population standard deviation. Each dot represents an event and is colored according to cluster membership. Cluster centers are marked by the "⊗" symbols.

leading EOFs (Figs. 3a,b), which together explain ~49% of the variance for the 79 events. Each event was represented by a point in the space, the coordinates of which correspond to the projection (i.e., dot product) of the anomaly field for the event onto the EOF patterns. Sensitivity tests (not shown) revealed that the clustering results are insensitive to inclusion of additional EOFs. Geopotential height data were obtained from the ECMWF ERA-Interim reanalysis dataset (ECMWF 2009; Dee et al. 2011) at 6-h intervals on a T255 (~0.7°) grid. Anomalies were calculated relative to daily means for 1979–2015 that were temporally smoothed by retaining only the first four harmonics of the annual cycle via a Fourier analysis.

Fuzzy clustering is similar to k-means clustering, commonly used in meteorology (e.g., Michelangeli et al. 1995), except that points do not belong to only one cluster but rather are assigned a coefficient indicating the strength of membership to each cluster. Cluster centers are calculated as the mean of all points weighted by this coefficient. As in Keller et al. (2011), the clustering was performed for an increasing number of

clusters starting at 2, and each solution was tested for stability by repeating the clustering 100 times, each time with different randomly placed initial cluster centers. Solutions that remained unchanged after the repetitions were considered stable. For stable solutions, each point was assigned to the cluster for which it had the strongest membership. The 2- and 4-cluster solutions were stable, and both identified distinct flow patterns (i.e., anomaly correlation coefficients of the composite height fields between the clusters were less than 0.4). The 4-cluster solution was deemed optimal because it captures more of the flow variability for the HPEs.

c. Composite analysis

Composite analyses, temporally centered on t_o, were constructed using the ERA-Interim to investigate the different HPE clusters. Anomalies were computed relative to the 1979–2015 daily climatological mean. The statistical significance of the anomalies was determined by performing a 1000-sample bootstrap test (Wilks 2011, his section 5.3.5) of the null

TABLE 1. Properties of the four clusters of long-duration HPEs: number of events, flow pattern description, event duration (days), and the maximum total precipitation accumulation (mm) in the Northern California domain. For duration and precipitation, the median is indicated by the first number, and the interquartile range is indicated in parentheses.

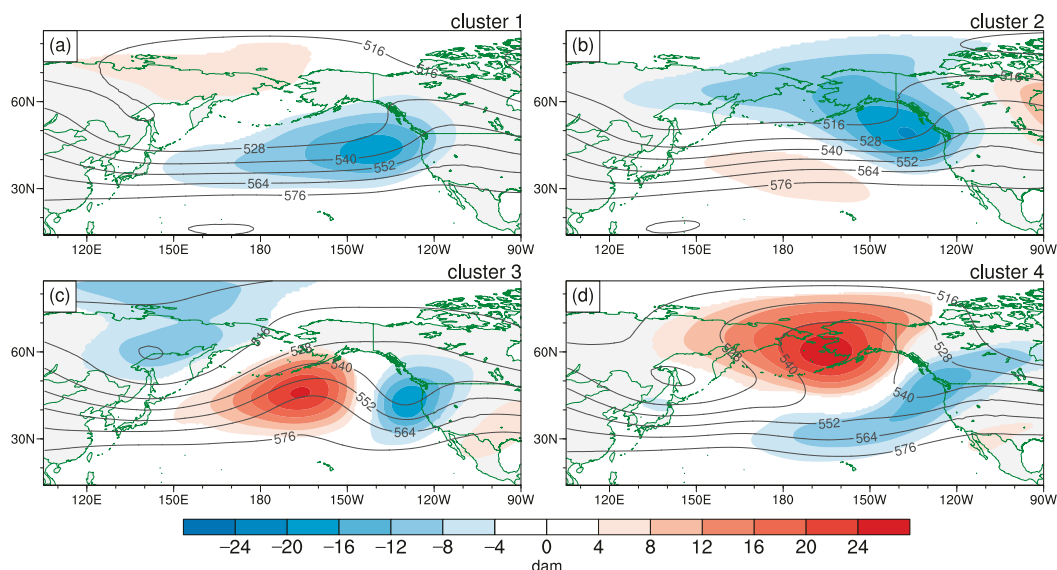| Cluster	No. of events	Flow pattern description	Duration (d)	Total precip. (mm)
1	28	Equatorward-shifted zonal jet	6 (5–8)	293.4 (251.1–363.0)
2	22	Poleward-shifted zonal jet	5 (4–6)	266.8 (221.7–364.7)
3	15	Midlatitude blocking	5 (4–6)	227.9 (175.3–269.6)
4	14	High-latitude blocking	6 (4–8)	336.2 (192.8–505.7)

FIG. 4. Composite analyses of (a)–(d) the four clusters of long-duration HPEs for the period from t_o to $t_o + 120$ h showing the time-mean 500-hPa geopotential height (contours every 12 dam) and geopotential height anomalies (dam; shading). Only statistically significant anomaly values are plotted.

hypothesis that the difference in the mean between the HPEs and the corresponding climatology is zero, with a significance level of 0.05 imposed.

Various diagnostics were computed in the composites. Analyses of potential temperature on the dynamic tropopause [defined as the 2-PV unit (PVU; 1 PVU $= 10^{-6}$ K kg^{-1} m^2 s^{-1}) surface] provide a PV perspective on the state of the tropopause-level flow and embedded jet streams. This field, referred to as θ_{DT}, is analogous to PV on a tropopause-intersecting isentropic surface, and positive and negative θ_{DT} anomalies relative to some reference state correspond to negative and positive PV anomalies, respectively (e.g., Morgan and Nielsen-Gammon 1998). Baroclinic instability was measured by the Eady growth rate maximum [Lindzen and Farrell 1980, their Eq. (28)], calculated for the 850–500-hPa layer following the method of Wernli et al. (2010, their section 2.2). Water vapor flux is quantified using the vertically integrated water vapor transport (IVT) vector, calculated for the 1000–300-hPa layer according to the method of Neiman et al. (2008). To diagnose synoptic-scale dynamically forced vertical motions, the **Q**-vector form of the quasigeostrophic (QG) ω equation [Hoskins et al. 1978, their Eq. (7)] was solved using a standard successive overrelaxation routine [Press et al. (2007), their section 20.5.1]. For the solution, boundary conditions were set to zero, the Coriolis parameter was set to the value at 45°N, and the static stability was set to a domain-averaged value.

Occurrences of breaking synoptic-scale Rossby waves, identified as elongated filamentary upper-level troughs called PV streamers (e.g., Wernli and Sprenger 2007), and extratropical cyclones were analyzed to further investigate the HPEs. Following the method of Wernli and Sprenger (2007), with minor modifications of Moore et al. (2019), PV streamers were identified in the ERA-Interim data on tropopause-intersecting isentropic surfaces (i.e., 310, 320, and

330 K) as coherent regions of high PV (>2 PVU) delimited by a segment of the 2-PVU contour whose endpoints are separated by a great-circle distance of <1000 km and by an along-contour distance of >3000 km. Streamers are categorized based on tilt relative to a zonal baseline. Streamers with a positive tilt ($\leq 75°$) indicate anticyclonic wave breaking, and streamers with a negative tilt ($\geq 105°$) indicate cyclonic wave
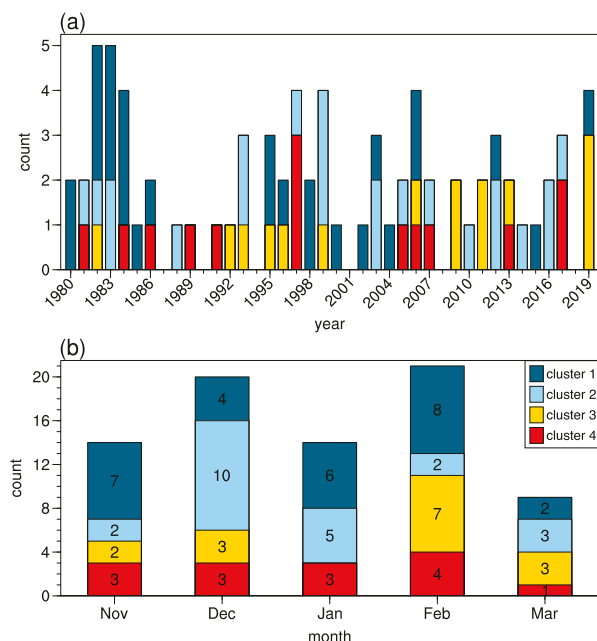

FIG. 5. The number of long-duration HPEs occurring in (a) in each extended winter season (tick marks indicate the ending year) and (b) each month. Bars are colored according to the legend in (b) to indicate the number of events for each cluster.
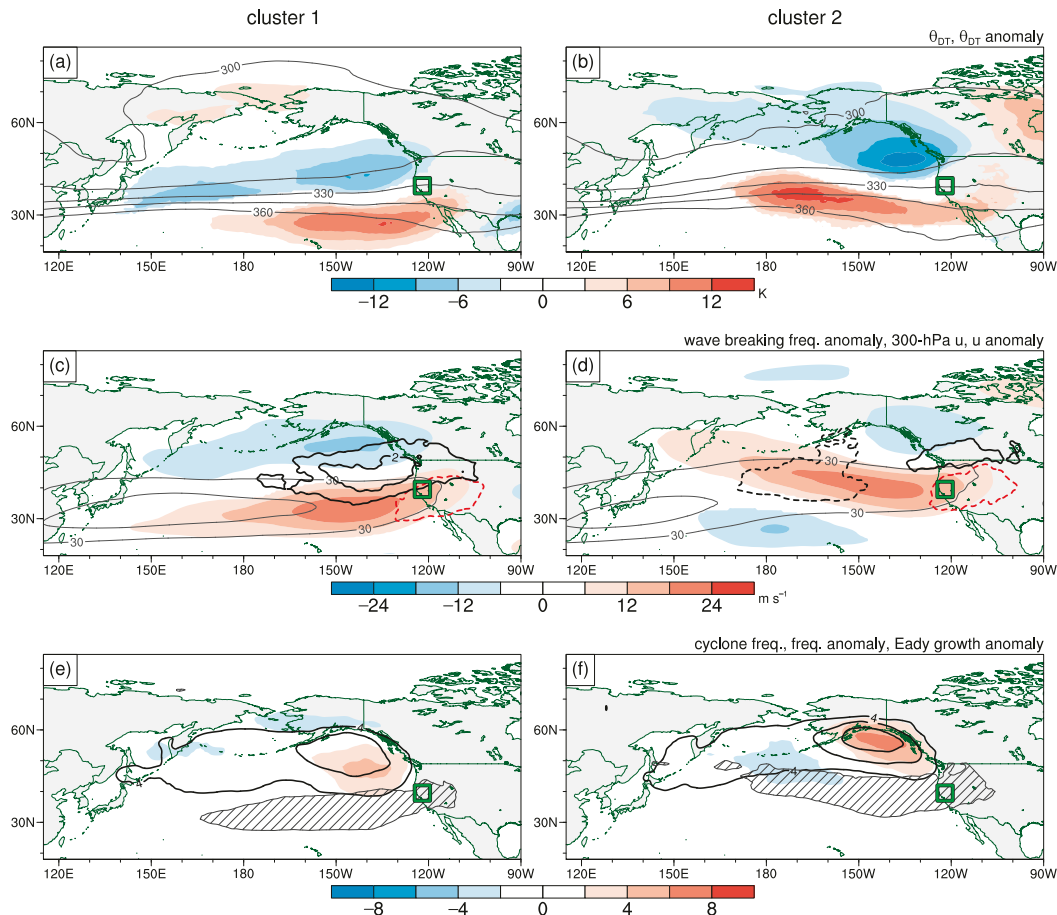
FIG. 6. Composite analyses of the (left) 28 HPEs in C1 and (right) 22 HPEs in C2 for the period from t_o to $t_o + 120$ h. (a),(b) Time-mean θ_{DT} (gray contours every 15 K) and θ_{DT} anomalies (K; shading). (c),(d) Time-mean 300-hPa zonal wind (gray contours every 10 m s^{-1} starting at 30 m s^{-1}) and 300-hPa zonal wind anomaly (m s^{-1}; shading) overlaid by absolute frequency anomalies of PV streamers (contours in increments of 1, dashed for negative values; cyclonic and anticyclonic wave breaking indicated in black and red, respectively). (e),(f) Absolute frequency (black contours in increments of 4) and absolute frequency anomalies (shading) of cyclones overlaid by time-mean 850–500-hPa Eady growth rate anomalies (hatching for values ≥ 0.1 day^{-1}). Only statistically significant anomaly values are plotted. The green box denotes the Northern California domain.

breaking. Following Wernli and Schwierz (2006), cyclones were identified and tracked as regions delimited by a closed sea level pressure contour surrounding a local sea level pressure minimum. The streamer and cyclone data were analyzed in the form of 6-h 1° latitude–longitude binary fields.

Composite maps were constructed for the absolute frequency of PV streamers and cyclones for all 6-h times between t_o and $t_o + 120$ h. The null hypothesis that the frequency is no different from that due to random chance was tested using a Monte Carlo approach. Specifically, the frequency map for a given HPE cluster was compared to a distribution of 1000 randomly generated frequency maps. Each random map was constructed using N randomly selected 5-day periods, where N is the sample size of the particular cluster. The start day of each random period was selected from the same months in which the HPEs occurred. A frequency value was considered statistically significant if it resided in the top or bottom 2.5% of the Monte

Carlo distribution. Frequency anomalies were computed by subtracting the mean of the Monte Carlo distribution.

3. Analysis of long-duration HPEs in Northern California

In this section, the results of the EOF analysis/fuzzy clustering and the composite analyses are presented. The composites reveal key characteristics of the HPE clusters and highlight factors contributing to prolonged heavy precipitation in Northern California.

a. Overview of the HPE clusters

The leading two EOFs of the 500-hPa geopotential height anomaly fields for the long-duration HPEs are shown in Figs. 3a,b. The first EOF exhibits a meridional dipole structure, with extrema at high and low latitudes, respectively, over the
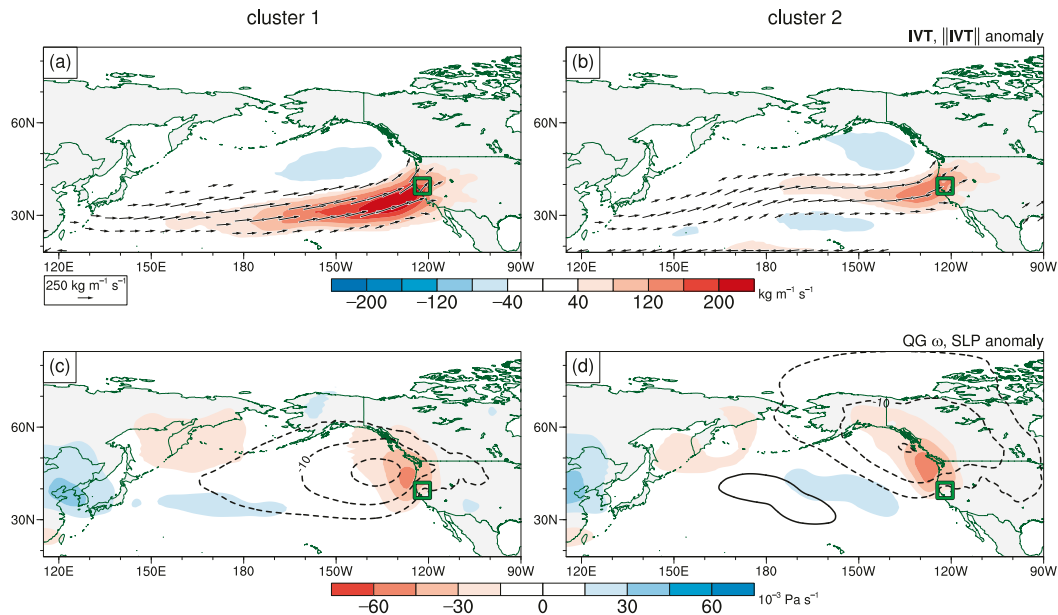
FIG. 7. Composite analyses of the (left) 28 HPEs in C1 and (right) 22 HPEs in C2 for the period from t_o to $t_o +$ 120 h. (a),(b) Time-mean IVT vectors [plotted for magnitudes ≥ 150 kg m^{-1} s^{-1}; reference vector below (a)] and IVT magnitude anomaly (kg m^{-1} s^{-1}; shading). (c),(d) Time-mean sea level pressure anomalies (black contours every 5 hPa, dashed for negative values) and 800–500-hPa layer-averaged QG vertical motion (10^{-3} Pa s^{-1}; shading). Only statistically significant anomaly values are plotted. The green box denotes the Northern California domain.

North Pacific, while the second EOF exhibits a large region of variability centered at midlatitudes over the eastern North Pacific. Four clusters of events, hereinafter referred to as C1, C2, C3, and C4, comprising 28, 22, 15, and 14 events, respectively, were identified (Fig. 3c; Table 1). C1 and C2 correspond to negative projections onto EOFs 2 and 1, respectively, and exhibit expansive negative geopotential height anomalies at middle and high latitudes over the North Pacific, with a negatively tilted trough positioned off the western coast of North America (Figs. 4a,b). These patterns are indicative of a strong zonal jet stream across the eastern North Pacific. The negative anomalies for C1 are zonally elongated and confined in the 30°–60°N band (Fig. 4a), whereas those for C2 exhibit a northwest–southeast tilt and extend to high latitudes (>60°N; Fig. 4b). C3 and C4, which together contain far fewer events than C1 and C2 (29 events compared with 50 events), correspond to positive projections onto EOFs 2 and 1, respectively. Accordingly, these clusters are characterized by a high-amplitude wave pattern exhibiting a prominent ridge, indicative of blocking, centered over the central North Pacific (Fig. 4c) and the Bering Sea–Alaska region (Fig. 4d), respectively. An elongated positively tilted trough is positioned near the North American coast on the eastern flank of the ridge.

The patterns in Fig. 4 bear some resemblance to previously documented flow patterns over the North Pacific and western North America. For example, the patterns for C1, C2, C3, and C4 are somewhat consistent with patterns for zonal extensions, poleward shifts, zonal retractions, and equatorward shifts, respectively, of the North Pacific jet (e.g., Winters et al. 2019, their Fig. 5), as well as different recurrent weather regimes over the Pacific–North America

region (e.g., Robertson and Ghil 1999, their Fig. 4). The patterns also resemble patterns found to favor landfalling atmospheric rivers along the West Coast (Guirguis et al. 2019, their Fig. 2).

Figure 5a depicts substantial interannual variability in the frequency and cluster membership of the HPEs. Some years experienced several events, whereas many others experienced one or zero. Serial occurrence of several events in a season can culminate in large hydrometeorological impacts, as occurred during the winters of 1982–83 (Quiroz 1983) and 2016–17 (White et al. 2019), which had five and three events, respectively. Figure 5b shows monthly variability for the HPEs. In aggregate, the events occurred most often in February and least often in March (Fig. 5b). Additionally, C1, C3, and C4 events occurred most often in February, whereas the C2 events occurred most often in December. Investigation of factors accounting for interannual and monthly variability of the HPEs is outside the scope of the current study and is left for future work.

b. Large-scale characteristics of the HPE clusters

Characteristics of the four HPE clusters are examined through composite analyses for the period from t_o to $t_o + 120$ h (Figs. 6–9). The pairs of clusters associated with zonal jet (C1 and C2) and blocking (C3 and C4) type patterns are discussed separately.

1) ZONAL JET PATTERNS

The patterns for C1 (Figs. 6a,c) and C2 (Figs. 6b,d) feature a negatively tilted upper-level trough, marked by negative θ_{DT} anomalies, off the western coast of North America and an anomalously strong, zonally extensive upper-level jet across
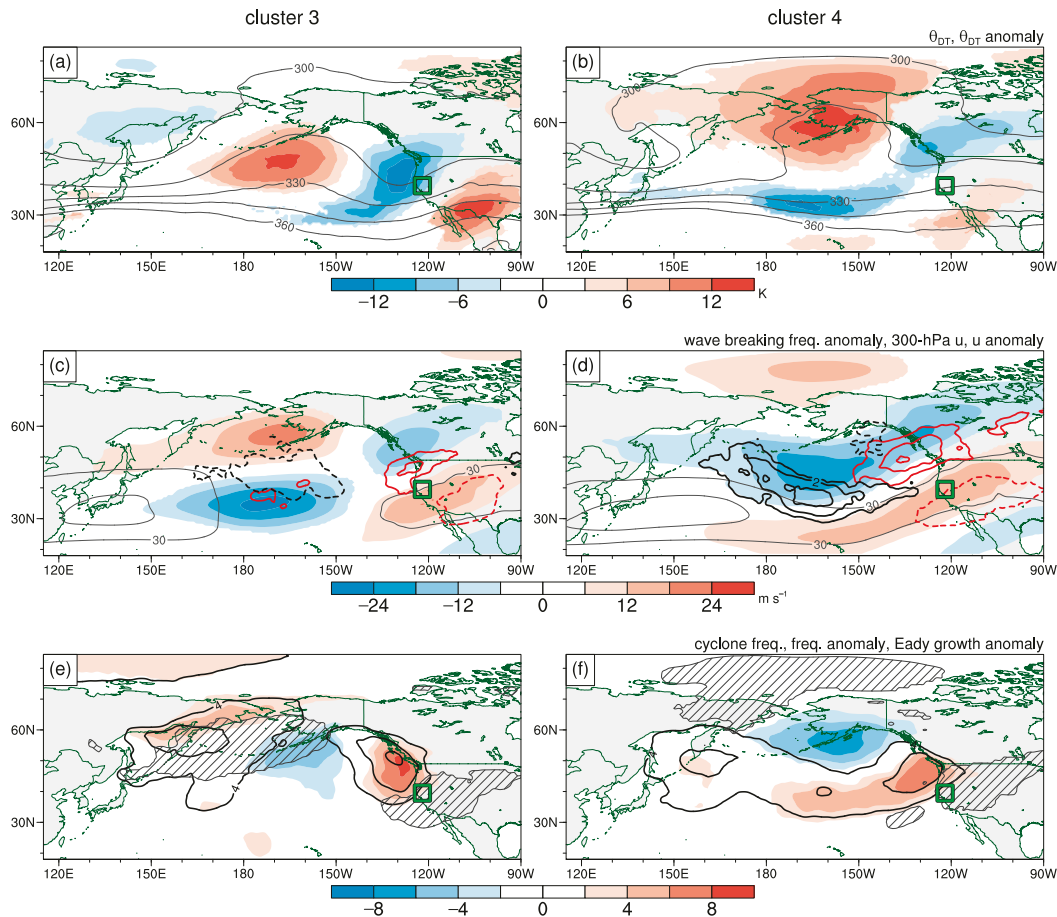
FIG. 8. As in Fig. 6, but for the (left) 15 HPEs in C3 and (right) 14 HPEs in C4.

the North Pacific associated with a negative–positive θ_{DT} anomaly couplet. The anomalous wind speeds in the jet coincide with enhanced lower-/midtropospheric baroclinicity, as indicated by positive Eady growth rate anomalies (Figs. 6e,f). The respective jets for C1 and C2 exhibit a zonal (Fig. 6c) and a northwest–southeast (Fig. 6d) orientation, with the latter being positioned at higher latitudes. The jet in each pattern connotes a corridor for propagation of upper-level Rossby waves and surface cyclones over the eastern North Pacific. For both clusters, a storm track, denoted by a region of 5-day absolute cyclone frequencies of ≥4, occurs on the poleward flank of the jet (Figs. 6e,f). A corridor of IVT is positioned on the equatorward flank of this storm track and is directed into California (Figs. 7a,b), reflecting moist flow in the warm sectors of the cyclones. Cyclone frequencies are maximized and significantly enhanced relative to climatology (Figs. 6e,f) near the θ_{DT} anomaly minimum (Figs. 6a,b) in the poleward jet exit region (Figs. 6c,d). The anomalous cyclone frequencies suggest a tendency for serial clustering of cyclones during the 5-day period. For both C1 and C2, anomalously high cyclonic wave breaking frequencies also occur in the poleward jet exit region (Figs. 6c,d), reflecting a tendency for upper-level waves along the jet to undergo a cyclonic wrap-up in conjunction with cyclogenesis. The cyclonic wave breaking anomalies are

considerably larger and more expansive for C1 (Fig. 6c) than for C2 (Fig. 6d).

The anomalous cyclone frequencies for C1 and C2 are related to expansive negative sea level pressure anomalies over the eastern North Pacific and western North America (Figs. 7c,d), indicating anomalous southwesterly lower-tropospheric geostrophic flow directed into the California coast. This flow is consistent with anomalously strong southwesterly IVT (Figs. 7a,b), indicative of landfalling atmospheric rivers linked to the cyclones. The anomalous IVT is stronger and more extensive for C1 than for C2. For both C1 and C2, upward QG vertical motion in the 800–500-hPa layer linked to the cyclone activity occurs in the poleward jet exit region over a broad area that includes Northern California (Figs. 7c,d).

2) BLOCKING PATTERNS

The patterns for C3 (Fig. 8a) and C4 (Fig. 8b) exhibit an elongated positively tilted trough positioned near the North American coast immediately downstream of a prominent blocking ridge. Analyses of blocking occurrences (not shown) identified according to the method of Schwierz et al. (2004) confirm that C3 and C4 events characteristically involve blocking. In both composites, the trough coincides with anomalous anticyclonic wave breaking frequencies (Figs. 8c,d),
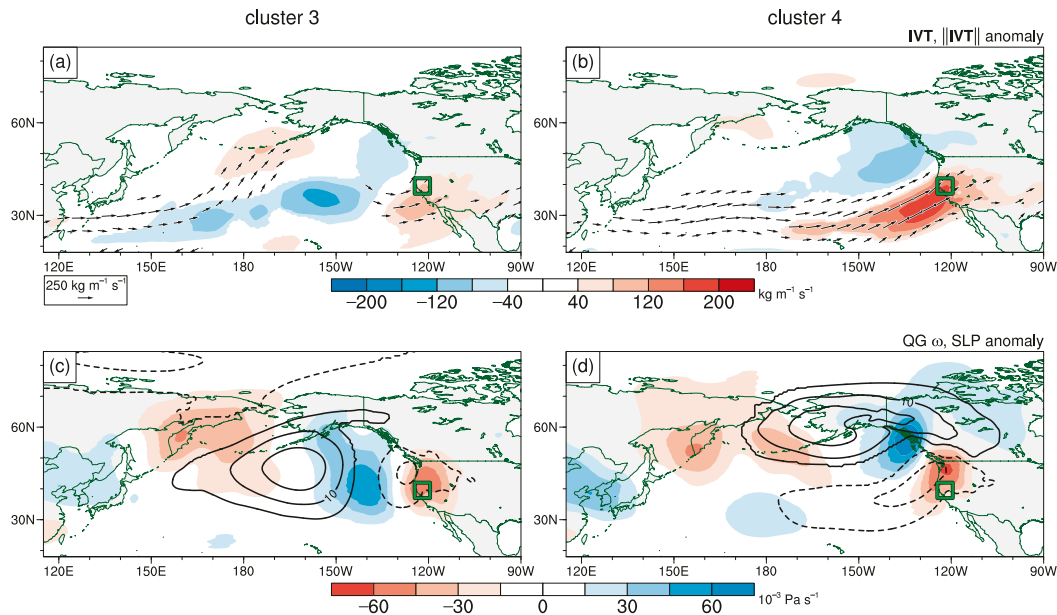
FIG. 9. As in Fig. 7, but for the (left) 15 HPEs in C3 and (right) 14 HPEs in C4.

and is flanked downstream by an anomalous upper-level jet and an associated baroclinic zone (Figs. 8e,f). Positive cyclone frequency anomalies (Figs. 8e,f) are focused in the region of wave breaking immediately poleward of the jet. For both C3 (Fig. 9c) and C4 (Fig. 9d), QG ascent is forced downstream of the trough over Northern California. The cyclone activity is manifested by negative sea level pressure anomalies (Figs. 9c,d) and anomalous southwesterly IVT directed into California (Figs. 9a,b). The cyclone frequency anomalies, sea level pressure anomalies, and IVT anomalies are more spatially extensive for C4 than for C3 (Figs. 8e,f, 9a–d). Moreover, the IVT is considerably stronger for C4.

The pattern for C4 (Figs. 8b,d), in contrast to that for C3 (Figs. 8a,c), exhibits a higher-latitude, omega-shaped blocking configuration with an anomalous upper-level jet and an associated zonal band of negative θ_{DT} anomalies stretching across the central and eastern North Pacific equatorward of the ridge (~30°–40°N). On the poleward flank of this jet, an elongated region of anomalous cyclonic wave breaking frequencies stretches from the upstream flank of the block toward the region of anticyclonic wave breaking near the British Columbia coast (Fig. 8d). This composite pattern is suggestive of phasing and interaction of cyclonically breaking waves (i.e., negatively tilted PV streamers) stretching across the midlatitude North Pacific from the upstream flank of the block with anticyclonically breaking waves (i.e., positively tilted PV streamers) on the downstream flank of the block, as documented by Moore et al. (2020). This situation favors an elongated storm track (Fig. 8f) and IVT corridor (Fig. 9b) stretching across the North Pacific into the British Columbia/northwestern U.S. coast.

c. Conditions over Northern California

For all four clusters, synoptic-scale ingredients for heavy precipitation, namely QG ascent and anomalous IVT, occur

over Northern California. Figure 10 demonstrates that, in the presence of these ingredients, the largest precipitation totals are focused over mountainous regions, especially the Coast Ranges and the Sierra Nevada (see Fig. 2a). These precipitation patterns are indicative of orographic forcing as the southwesterly IVT (Table 2; Figs. 7a,b, 9a,b) impinges on the terrain. The events in all clusters are characterized by extended periods of heavy precipitation (median duration of 5–6 days; Table 1). In general, C1 and C4 are characterized by longer event durations and higher precipitation totals than C2 and C3 (Table 1; Fig. 10). Additionally, C1 and C4 tend to involve larger column-integrated water vapor and IVT in the vicinity of Northern California than C2 and C3 (Table 2). The higher precipitation and more moist conditions for C1 and C4 than for C2 and C3 are consistent with the stronger, more elongated IVT corridors directed into California in the C1 and C4 composites (Figs. 7a,b, 9a,b). The blocking clusters (C3 and C4) tend to be associated with stronger QG ascent over the Northern California domain than the zonal jet clusters (C1 and C2; Table 2).

d. Persistence of the flow patterns

Composite Hovmöller diagrams in Fig. 11 summarize the evolution of the flow for the long-duration HPEs. An important caveat here is that the compositing only captures portions of wave signals that are in-phase for the constituent events and thus precludes realistic depiction of individual synoptic-scale waves. Diagrams of 500-hPa geopotential height anomalies (Figs. 11a–d) highlight the general coherence and persistence of the large-scale patterns for the four clusters. In each pattern, negative anomalies are maintained over the eastern North Pacific in the vicinity of the U.S. coast during the ~4–8 days following t_o (Figs. 11a–d). For C3 (Fig. 11c), these negative anomalies occur immediately
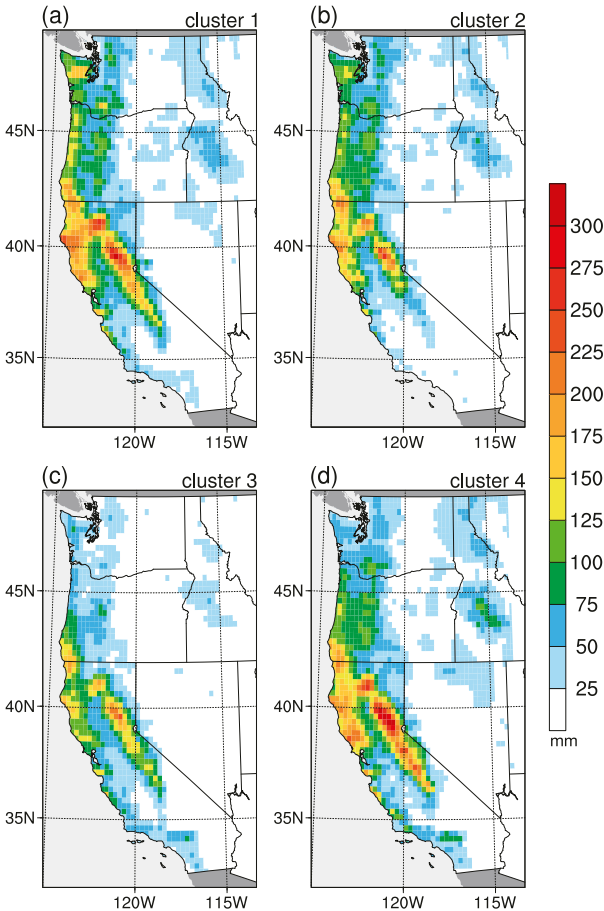
FIG. 10. The median total precipitation (mm) associated with the HPEs in (a)–(d) C1–C4.

clustering of landfalling cyclones and atmospheric rivers for the HPEs. The median count of discrete cyclones overlapping a box near the coast (35°–50°N, 124°–130°W) between $t_o - 24$ h and $t_o + 144$ h is four for C1, C2, and C4, and three for C3, respectively (Table 2). Based on Monte Carlo tests (see section 2c), these 7-day counts are significantly greater than the count expected due to random chance and therefore suggest a tendency for cyclone clustering.

e. Analog-based analysis

The flow patterns that have been examined thus far could have practical utility for detecting Northern California HPEs in numerical weather model forecasts or general circulation model simulations, particularly those that poorly represent precipitation. For such applications, it is necessary to determine: 1) whether the occurrence of a pattern resembling an HPE composite pattern is statistically associated with an elevated likelihood of an HPE, and 2) what factors distinguish patterns that result in long-duration HPEs from patterns that do not. To address these issues, analogs for each HPE cluster were identified based on an analog index, calculated by projecting the mean 500-hPa geopotential height anomaly field for each day during November–March 1979–2019 onto the corresponding composite field (Fig. 4). For each cluster, analogs were selected as days with an index value in the top 5% (top 308 days) of all index values for the cluster.

The departure of the probability of heavy precipitation for a given set of analog days from the random or climatological probability was assessed using the Monte Carlo approach described in section 2c. For the four patterns, ratios of the probability for the analogs to the random probability are well in excess of unity and statistically significant over California as well as many other parts of the western United States (Figs. 12a–d). Ratios computed for heavy precipitation occurring as part of a long-duration (≥ 3 days) sequence yield generally similar results but substantially higher values (Figs. 12e–h). Overall, these results demonstrate statistically significant increases in the likelihood of HPEs, especially those with a long duration, when an analog pattern occurs. The ratios exceeding unity for the C1 (Figs. 12a,e) and C2 (Figs. 12b,f) analogs cover large portions of California and the northwestern United States, whereas those for the C3 (Figs. 12c,g) and C4 (Figs. 12d,h) analogs are generally confined to California. For C3, the >1 ratios of long-duration

downstream of a quasi-stationary ridge (axis at ~170°W). For C4 (Fig. 11d), the negative anomalies occur equatorward of a long-lived high-latitude ridge that appears to propagate slowly westward.

The persistent negative height anomalies near the U.S. coast in each composite generally coincide with positive IVT anomalies near the U.S. coast (Figs. 11a–d). The persistence of the height and IVT anomalies is consistent with serial

TABLE 2. Atmospheric conditions for the four clusters of long-duration HPEs: the area-averaged time-mean 800–500-hPa layer-averaged QG vertical motion (10^{-3} Pa s^{-1}; multiplied by -1 so that positive values indicate ascent) in the Northern California domain from $t_o + 0$ h to $t_o + 120$ h; the area-averaged time-mean IVT magnitude (kg m^{-1} s^{-1}), IVT direction (meteorological definition; degrees), and column-integrated water vapor (mm) in a box off the California coast (32°–42°N, 124°–130°W) from $t_o + 0$ h to $t_o + 120$ h; and the number of discrete cyclones that overlapped a larger box off the coast (35°–50°N, 124°–130°W) between $t_o - 24$ h and $t_o + 144$ h. The median is indicated by the first number, and the interquartile range is indicated in parentheses.

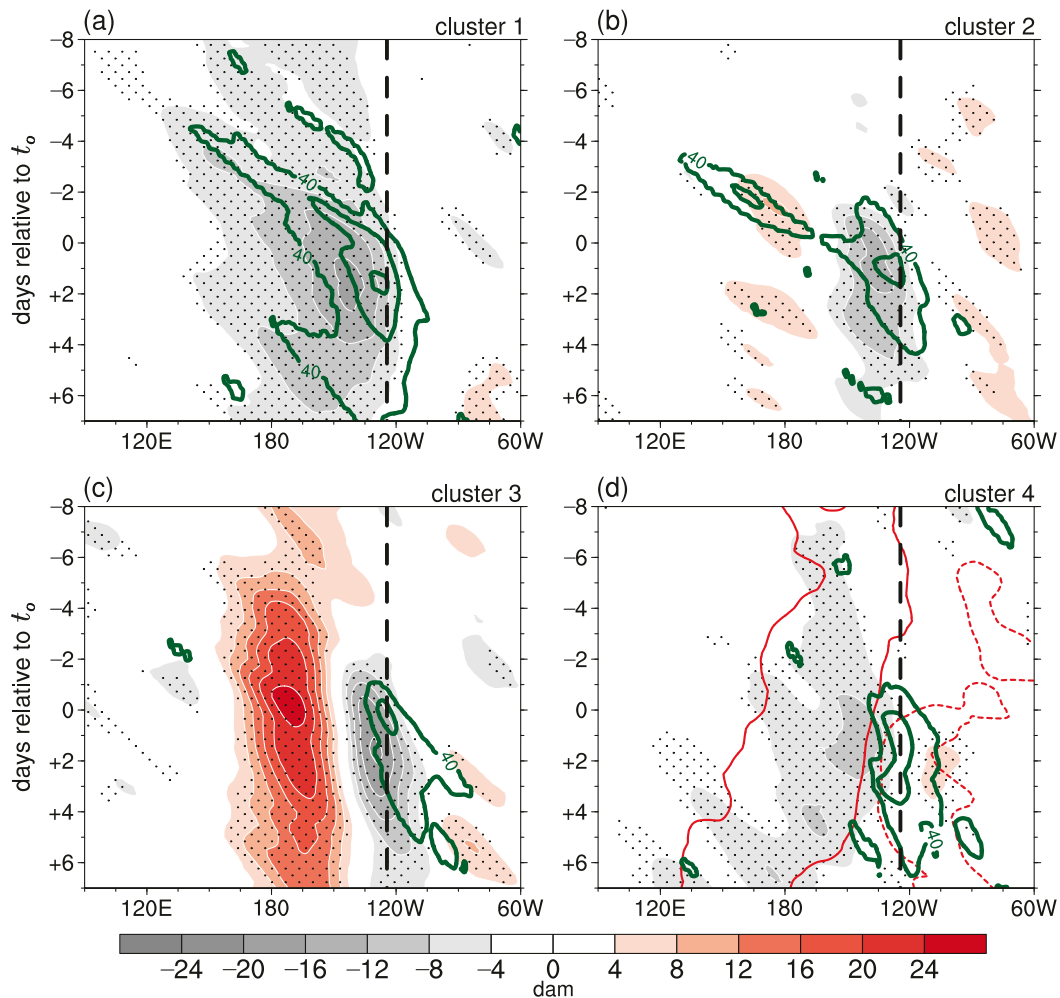| Cluster	QG vertical motion (10^{-3} Pa s^{-1})	IVT magnitude (kg m^{-1} s^{-1})	IVT direction (°)	Integrated water vapor (mm)	Number of discrete cyclones
1	27.5 (12.0–43.8)	344.8 (317.9–426.6)	238.4 (227.4–253.3)	21.2 (19.8–23.1)	4 (2–4)
2	15.9 (0.6–27.6)	288.8 (262.6–335.2)	250.4 (240.1–255.5)	18.9 (16.9–20.3)	4 (2–5)
3	47.9 (35.5–65.7)	228.0 (189.9–246.0)	237.4 (227.6–245.7)	15.7 (13.0–17.2)	3 (3–5)
4	40.7 (27.4–47.5)	343.1 (269.5–416.2)	239.8 (232.0–246.1)	19.9 (18.2–23.0)	4 (3–5)

FIG. 11. Composite Hovmöller diagrams from $t_o − 8$ days to $t_o + 7$ days for the HPEs in (a)–(d) C1–C4 showing 500-hPa geopotential height anomalies (dam; shading; stippling denotes statistically significant values) averaged in the (a),(b) 30°–50°N, (c) 35°–55°N, and (d) 20°–40°N bands overlaid by IVT magnitude anomalies (green contours every 40 kg m^{-1} s^{-1} starting at 40 kg m^{-1} s^{-1}; only statistically significant values plotted) averaged in the 25°–45°N band. In (d), geopotential height anomalies averaged in the 45°–65°N band are contoured in red (6- and −6-dam contours only) to represent the high-latitude blocking pattern. The vertical dashed line marks the western boundary of the Northern California domain.

sequences are mostly concentrated in southern rather than Northern California. This result could reflect occurrences of meridionally elongated troughs off the U.S. coast that may be especially conducive to HPEs in southern California.

For each pattern type, a sample of analogs for which a long-duration HPE occurred at any grid point in the Northern California domain was compared in a composite framework with a sample of null analogs for which a long-duration HPE did not occur at any point in the domain nor within 4° latitude of the domain bounds. Analogs that occurred on consecutive days were considered to comprise the same analog case. Final samples of 41, 37, 28, and 25 HPE cases and 26, 29, 34, and 37 null cases were identified for C1, C2, C3, and C4, respectively. In the composites, t_A refers to 0000 UTC on the first day of the cases. The null hypothesis that the difference in the mean

between the HPE and null samples is zero was tested via a 1000-sample bootstrap test, with a significance level of 0.05. For geopotential height and IVT, the climatological mean was removed prior to computing differences. Significant HPE-minus-null case differences are displayed in Fig. 13.

For C1 (Fig. 13a) and C2 (Fig. 13c), the negative 500-hPa geopotential height anomalies over the eastern North Pacific in the HPE composite are larger and shifted to the east compared with those in the null composite, indicating a stronger and more zonally elongated jet stream extending into the U.S. coast. Accordingly, for both C1 (Fig. 13b) and C2 (Fig. 13d) the corridor of cyclone activity for the HPE cases is shifted to the east of that for the null cases such that cyclone frequencies are significantly higher off the British Columbia/southern Alaska coast for the HPE cases. Consistent with these differences, the
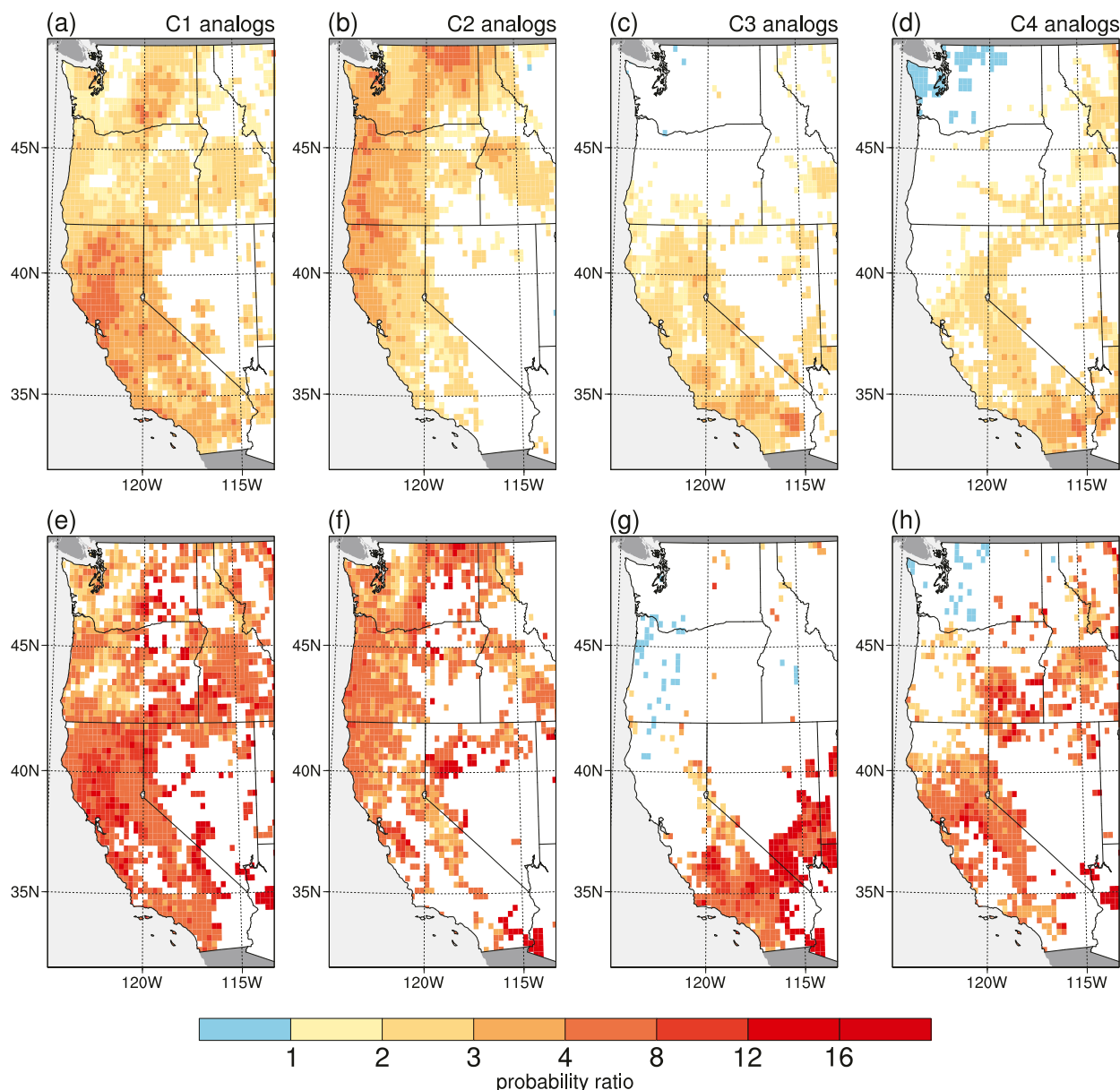
FIG. 12. (a)–(d) Ratio of the probability of heavy precipitation (thresholds shown in Fig. 1a) on analog days for C1–C4 to the random probability. (e)–(f) As in (a)–(d), but for heavy precipitation occurring as part of a long-duration (≥3 days) sequence. Grid cells for which the ratio is not statistically significant are shaded in white.

HPE cases exhibit significantly stronger IVT directed into California compared with the null cases (Figs. 13b,d).

For C3 (Fig. 13e) and C4 (Fig. 13g), phase differences are evident in the geopotential height anomaly patterns over the eastern North Pacific and western North America between the HPE cases and null cases. In the HPE composite, large negative anomalies (i.e., a trough) on the eastern flank of the blocking ridge are positioned off the U.S. coast, whereas in the null composite the negative anomalies are positioned farther downstream over western and central North America. These phase differences reflect differences in the location of the anticyclonic wave breaking

(not shown) downstream of the blocking ridge. The negative height anomalies in vicinity of the U.S. coast for the C3 (Fig. 13f) and C4 (Fig. 13h) HPE cases support significantly higher cyclone frequencies over the eastern North Pacific and, thereby, stronger IVT into California compared with the corresponding null cases.

4. Case studies

Case studies are presented here to provide representative depictions of the different dynamical scenarios embodied in the composite analyses. For brevity, only two events
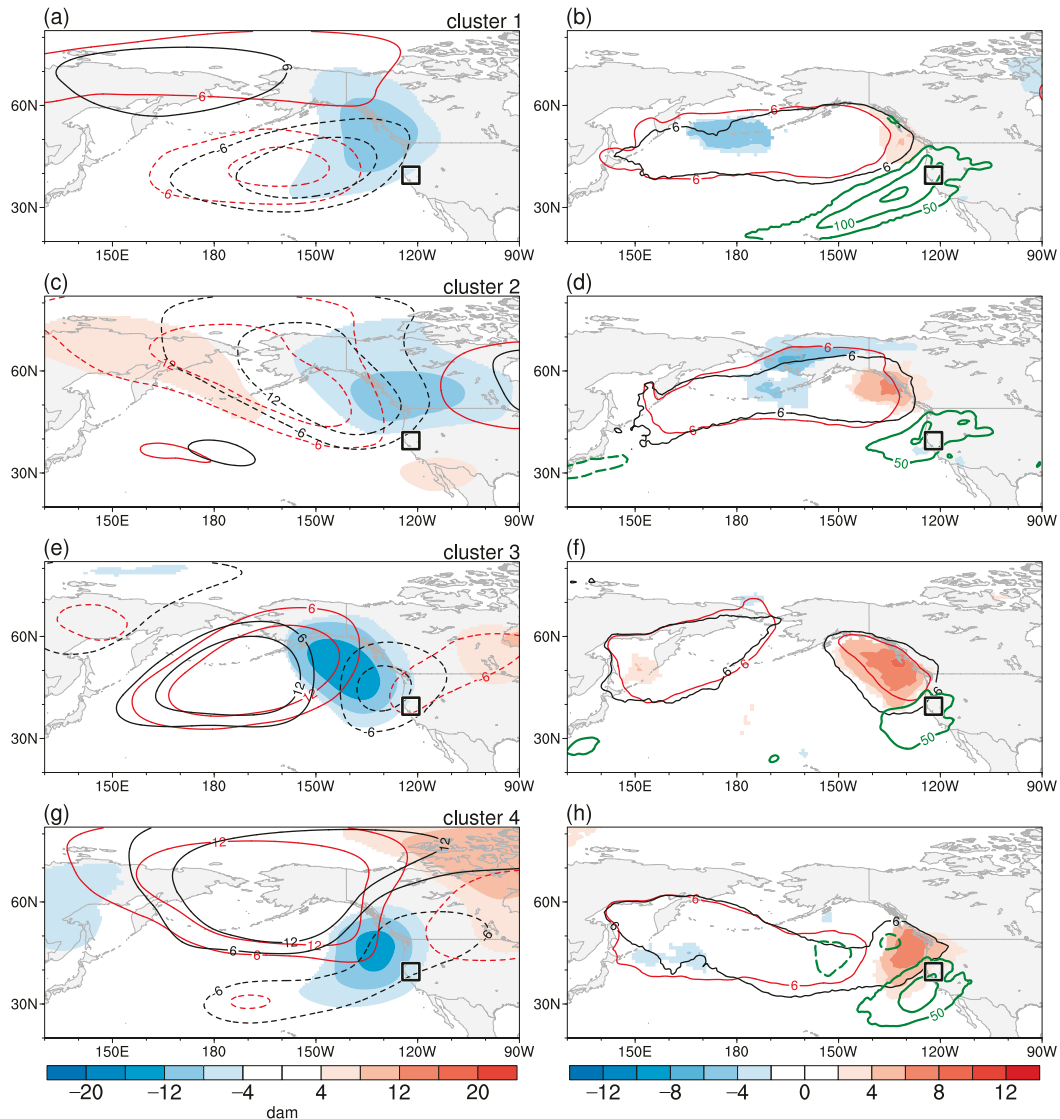
FIG. 13. Comparison of the HPE and null analog cases for (a),(b) C1; (c),(d) C2; (e),(f) C3; and (g),(h) C4 for the period from $t_A - 24$ h to $t_A + 144$ h. (left) Differences in the mean 500-hPa geopotential height (dam; shading) between HPE and null cases overlaid by the mean 500-hPa geopotential height anomalies (-12-, -6-, 6-, and 12-dam contours, dashed for negative values) for the null (red) and HPE (black) cases. (right) Differences in the mean absolute cyclone frequencies (shading) and the mean IVT magnitude (dark green contours every 50 kg m^{-1} s^{-1}, dashed for negative values) between the HPE and null cases overlaid by the mean absolute cyclone frequency (6-unit contour) for the null (red) and HPE (black) cases. Only statistically significant differences are plotted. The black box denotes the Northern California domain.

are examined: a C1 event during 4–15 January 1995 (Figs. 14 and 15) and a C4 event during 12–20 February 1986 (Figs. 16 and 17). These events produced the highest precipitation totals among the C1 and C4 events.

a. C1 case: January 1995

The C1 event, spanning 4–15 January 1995, produced widespread large precipitation totals (e.g., >200 mm) over Washington, Oregon, and California (Fig. 14a). The largest totals (e.g., >400 mm; local maxima > 800 mm) occurred in

Northern California, primarily over mountainous regions, and caused high-impact flooding (USGS 1995).

The time-mean large-scale pattern for the event (Fig. 14b) featured a mostly zonal upper-level jet stream across the North Pacific, as evidenced by a band of large θ_{DT} gradients between 30° and 40°N. A negatively tilted trough was positioned south of Alaska, signifying recurrent cyclonic Rossby wave breaking episodes throughout the event. A meridional negative–positive θ_{DT} anomaly couplet was established in association with the trough, implying an anomalous gradient and enhanced
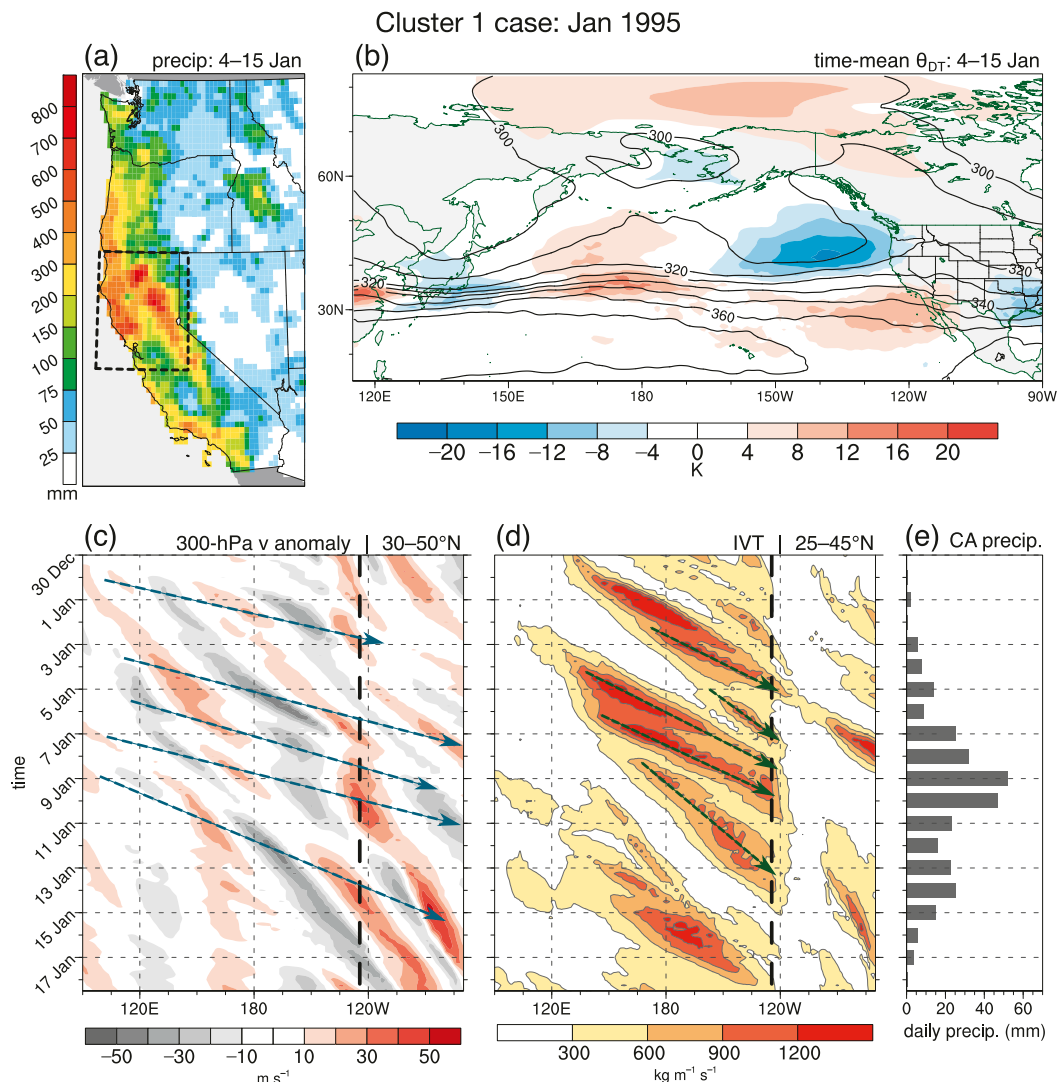
FIG. 14. Conditions during the Jan 1995 C1 event. (a) Accumulated precipitation (mm), and (b) time-mean θ_{DT} (black contours every 10 K) and θ_{DT} anomalies (K; shading) for 4–15 Jan 1995. The black box in (a) denotes the Northern California domain. Hovmöller diagrams of (c) 300-hPa meridional wind anomalies (m s^{-1}; shading) averaged in the 30°–50°N band and (d) the maximum IVT magnitude (kg m^{-1} s^{-1}; shading) in the 25°–45°N band, and (e) a time series of area-averaged daily precipitation in the Northern California domain for 30 Dec 1994–18 Jan 1995. Blue arrows in (c) indicate the approximate group velocity of subjectively identified Rossby wave packets discussed in the text. Green arrows in (d) denote IVT maxima linked to the landfalling cyclones discussed in the text. The vertical dashed line in (c) and (d) marks the western boundary of the Northern California domain.

westerly flow in the jet near the U.S. coast. The zonal jet was conducive to propagation of successive Rossby waves across the eastern North Pacific toward North America (Fig. 14c).

During the event, precipitation (Fig. 14e) was sustained by repeated periods of strong water vapor flux (Fig. 14d) linked to a series of five cyclones, labeled L1–L5 in Figs. 15a–h for 5–12 January 1995. The cyclones developed in conjunction with successive upper-level troughs propagating across the central and eastern North Pacific (Figs. 15a–h) in association with Rossby wave packets (Fig. 14c). As the

cyclones successively developed and approached the coast, the associated troughs underwent cyclonic wave breaking, manifested by cyclonic overturning of the θ_{DT} field (Figs. 15a–h).

Following the landfall of the initial cyclone on 5 January 1995 (Fig. 15a), the latter four cyclones moved across the eastern North Pacific into the U.S. coast in rapid succession during 6–12 January (Figs. 15b–g). Upon reaching the coast, each of the four cyclones slowed and followed an increasingly poleward track in conjunction with the cyclonic wave breaking aloft (Figs. 15b–g). The spatiotemporal clustering of these cyclones between 7 and
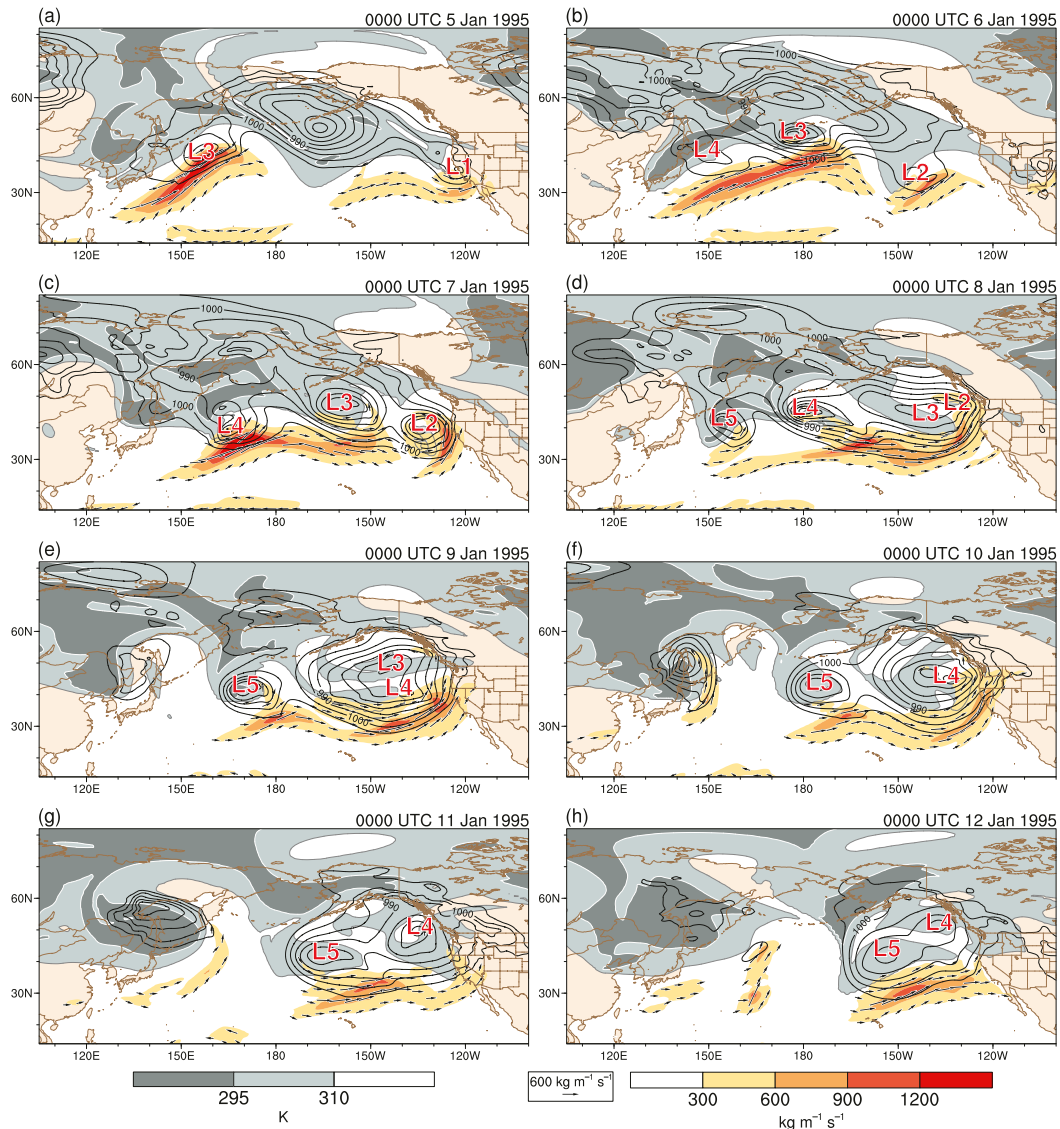
FIG. 15. The θ_{DT} (K; shading according to the left color bar), IVT magnitude (kg m^{-1} s^{-1}; shading according to the right color bar) and vectors (plotted for magnitudes $\geq$ 300 kg m^{-1} s^{-1} according to the vector scale), and sea level pressure (black contours every 5 hPa for values $\leq$ 1005 hPa) at 0000 UTC (a)–(h) 5–12 Jan 1995 (C1 event). The sea level pressure minima for the five cyclones associated with precipitation in the Northern California domain are labeled L1–L5.

15 January 1995 served to establish and maintain a larger-scale cyclonic circulation over the eastern North Pacific (Figs. 15c–h). The atmospheric rivers corresponding to the four cyclones, identifiable as IVT maxima, successively extended through the same corridor on the southern and eastern flank of this circulation (Figs. 15c–h), thereby maintaining nearly continuous water vapor flux into Northern California during 7–15 January (Fig. 14d).

b. C4 case: February 1986

The C4 event, spanning 12–20 February 1986, produced a generally similar precipitation distribution to the January 1995

event, though precipitation totals were larger along the Sierra Nevada mountains (Fig. 16a). This precipitation resulted in high-impact flooding throughout Northern California (NOAA/NWS/CNRFC 1986). The event involved a high-amplitude flow pattern (Fig. 16b) that closely resembles the C4 composite pattern (Fig. 8b). An expansive blocking ridge was centered over the Bering Sea and was flanked upstream and downstream by tilted troughs, signifying cyclonic and anticyclonic wave breaking, respectively. Additionally, a band of enhanced θ_{DT} gradients, connoting a jet stream, stretched across the North Pacific equatorward of the ridge.

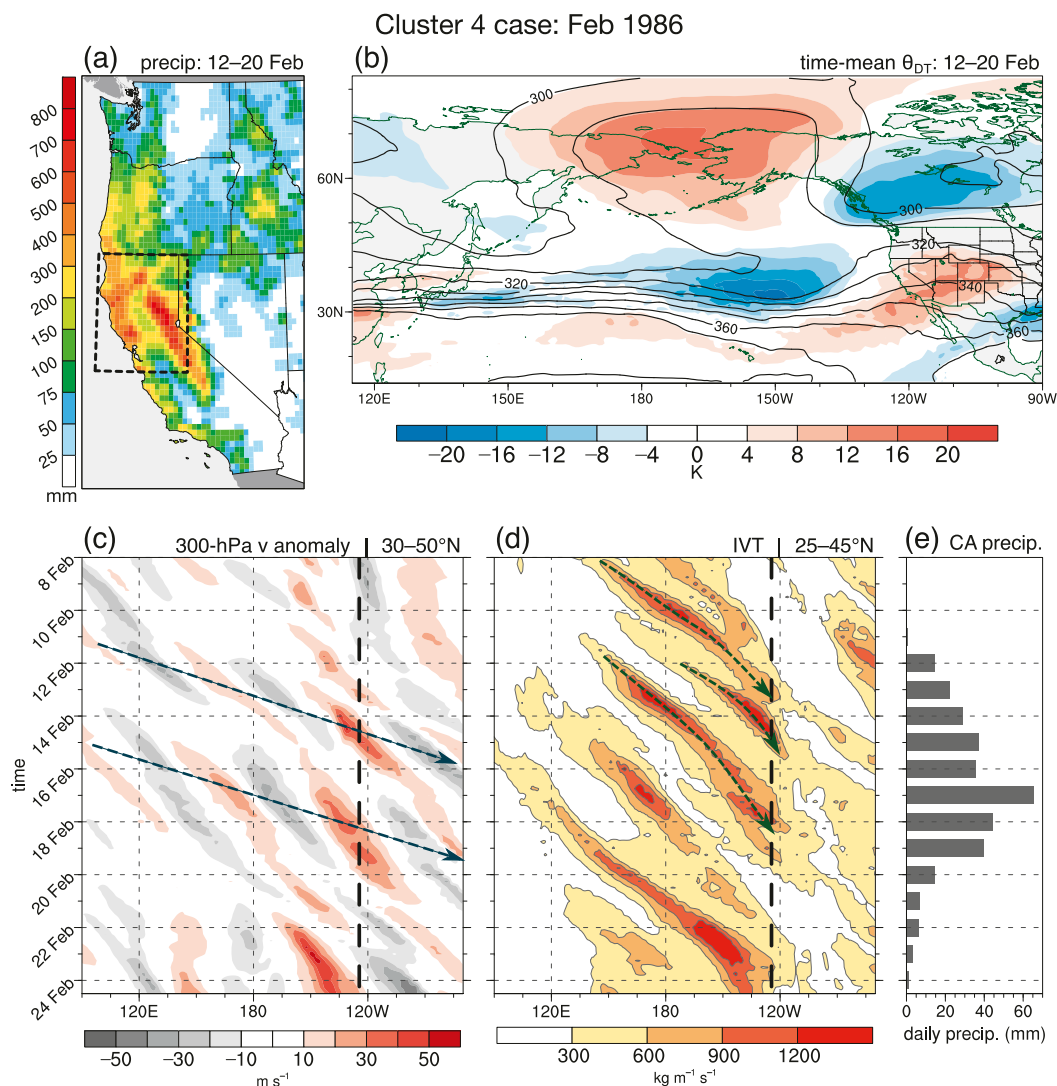## Cluster 4 case: Feb 1986

FIG. 16. As in Fig. 14, but for the Feb 1986 C4 event. Plots are shown for (a),(b) 12–20 Feb and (c)–(e) 8–24 Feb 1986.

The precipitation during the event (Fig. 16e) was sustained by repeated periods of strong water vapor flux (Fig. 16d) linked to a series of three cyclones, labeled L1–L3 in Figs. 17a–h for 12–19 February 1986. The cyclones developed in connection with successive negatively tilted upper-level troughs or PV streamers that stretched across the central and eastern North Pacific equatorward of the blocking ridge (Figs. 17a–h), as reflected by discrete eastward-moving meridional wind anomalies in Fig. 16c. These troughs formed through repeated cyclonic wave breaking on the upstream flank of the blocking ridge. The latter two troughs approached the U.S. coast on 14–16 February and 17–20 February, respectively (Figs. 17c–h), in association with two successive Rossby wave packets (Fig. 16c) along the jet equatorward of the block.

The first of the three cyclones followed a northwestward track over the eastern North Pacific between 12 and 13 February 1986 in conjunction with cyclonic wave breaking aloft (Figs. 17a,b). The associated atmospheric river made landfall on 13 February in association with a surface frontal trough extending southeast from the cyclone center (Fig. 17b). The latter two cyclones and their accompanying atmospheric rivers impacted California during 14–16 February and 17–20 February, respectively (Figs. 17c–h). The three atmospheric river-related surface disturbances each followed a similar path into the northwestern U.S. coast along a baroclinic zone (not shown) maintained through anticyclonic wave breaking downstream of the ridge (Figs. 17b–h). Consequently, the atmospheric rivers successively impacted Northern California (Figs. 16d, 17b–h).

5. Summary and conclusions

In this study, we constructed a climatology of long-duration HPEs, defined as quasi-continuous periods of heavy precipitation
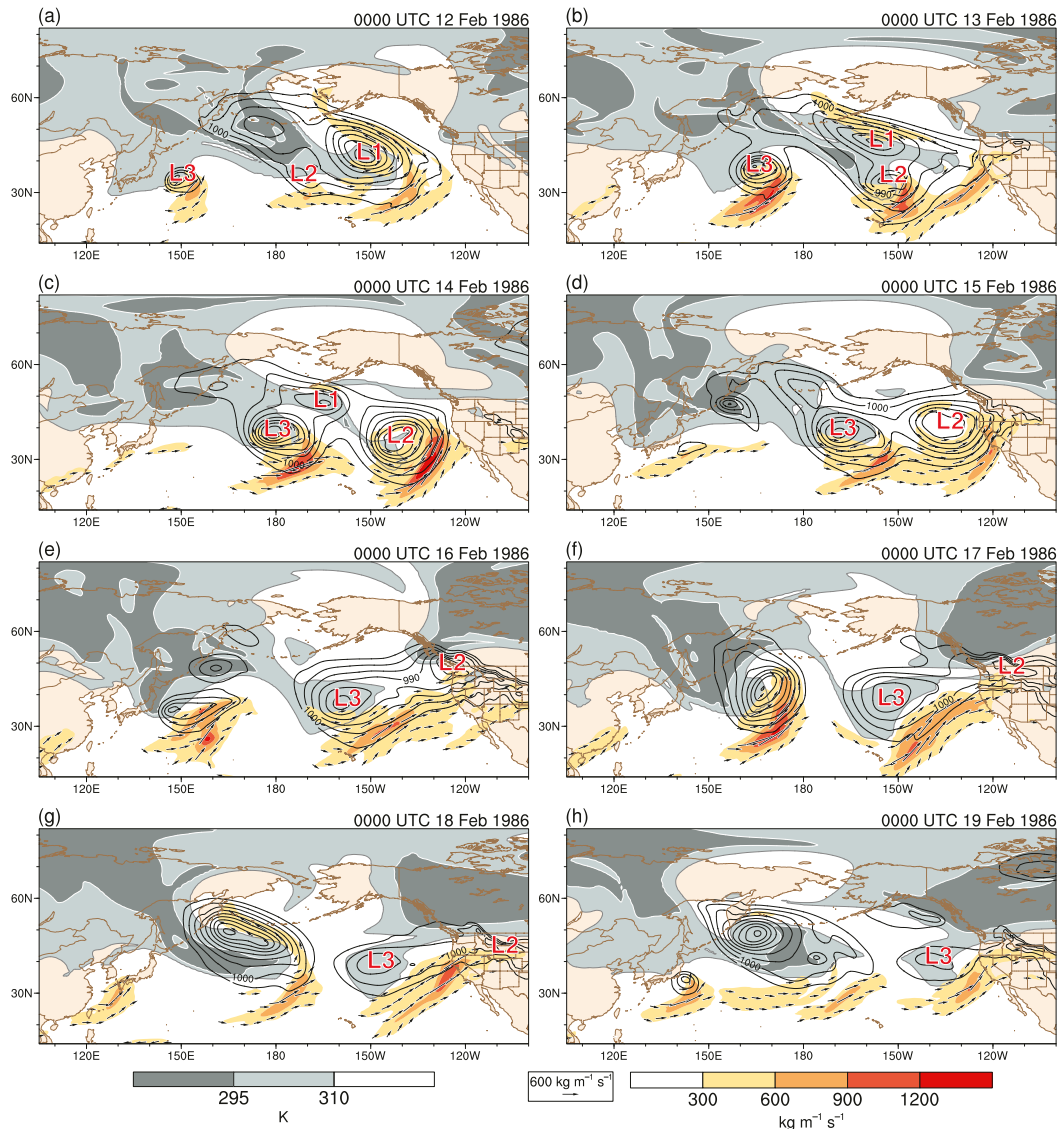
FIG. 17. As in Fig. 15, but for 12–19 Feb 1986 (C4 event). The sea level pressure minima for the three cyclones associated with precipitation in the Northern California domain are labeled L1–L3.

(daily precipitation exceeding the climatological 95th percentile) lasting for ≥3 days, over the United States for 1979–2019. In addition, we investigated flow patterns and dynamical processes associated with events over the West Coast, particularly Northern California, a region that is particularly susceptible to long-duration HPEs. Investigation of events in other regions is left for future work.

An objective flow-based categorization method involving EOF analysis and fuzzy clustering was applied to the 500-hPa geopotential height anomaly fields over the North Pacific and western North America for the selected events in order to identify principal patterns associated with long-duration HPEs. Four different event clusters (i.e., C1, C2, C3, and C4) were identified and examined through composite analyses as well as case studies of events in February 1986 and January

1995. The composites reveal four distinct large-scale flow patterns, schematically summarized in Fig. 18. The patterns all tend to be persistent, remaining in place for several days, and are characterized by quasi-stationary circulation anomalies that serve to maintain conditions for heavy precipitation in Northern California. For each cluster, an anomalous upper-level trough occurs in connection with Rossby wave breaking near the western coast of North America. The trough is associated with anomalous baroclinicity, anomalous extratropical cyclone frequencies, and QG ascent in the vicinity of Northern California. The cyclone activity is linked to persistent strong water vapor flux directed into Northern California, reflecting occurrences of landfalling atmospheric rivers that favors sustained orographic forcing of precipitation. The nexus of Rossby wave breaking and landfalling atmospheric rivers
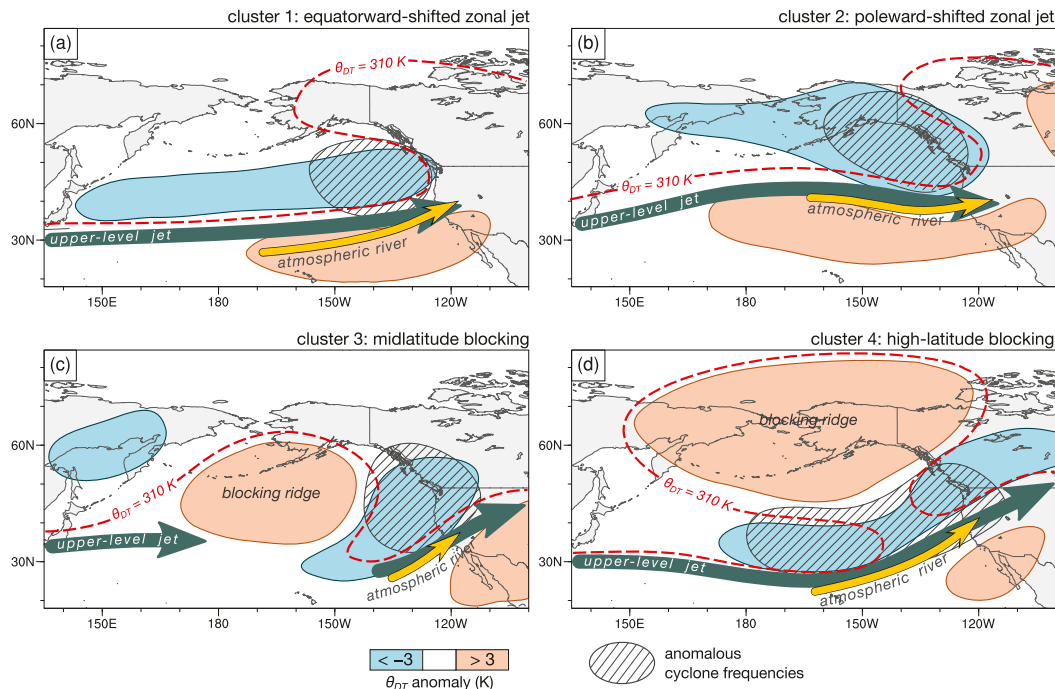
FIG. 18. Schematic illustrations summarizing key features of the large-scale flow patterns for (a)–(d) C1–C4. Plots show the θ_{DT} anomaly pattern (shading), the configuration of the upper-level jet stream (thick dark arrow), the corridor of anomalous IVT associated with atmospheric rivers (thin yellow arrow), the 310-K θ_{DT} isentrope (dashed red), and the region of anomalously high cyclone frequencies where cyclone clustering is favored (hatching).

along the West Coast revealed by the composites is consistent with findings of several prior studies (e.g., Ryoo et al. 2013; Mundhenk et al. 2016).

The results of the composite analyses and case studies indicate a tendency for serial clustering of synoptic-scale Rossby waves and extratropical cyclones near the U.S. coast during the HPEs. This clustering supports repeated periods of water vapor flux and forcing for ascent over Northern California and, thereby, constitutes an essential process for the prolongation of the heavy precipitation, as highlighted in prior case studies (e.g., Grams et al. 2014; Priestley et al. 2017a; Moore et al. 2020). The large-scale patterns embodied in the composites for the four HPE clusters appear to modulate the occurrence of higher-frequency synoptic-scale disturbances over the eastern North Pacific. The persistence of these patterns for several days fosters serial clustering of the disturbances.

The flow patterns identified for the four HPE clusters logically divide into two general types: one characterized by a strong, elongated zonal upper-level jet stream over the North Pacific (C1 and C2), and another by a high-amplitude wave pattern featuring blocking over either the central North Pacific (C3) or the Bering Sea–Alaska region (C4). The zonal jet-type HPEs occur much more frequently than the blocking-type HPEs. The two zonal jet patterns are primarily differentiated by the latitude and orientation of the jet stream; similarly, the two blocking patterns are primarily differentiated by the location and structure of the blocking ridge. In the zonal jet patterns (Figs. 18a,b), an anomalously strong jet extends across

the eastern North Pacific to the West Coast and corresponds to a persistent elongated waveguide and baroclinic zone. As illustrated in the January 1995 case study, synoptic-scale waves propagating along the jet induce cyclone development and undergo cyclonic wave breaking in the poleward jet exit region near the West Coast. Precipitation is sustained in Northern California by successive landfalling cyclones and atmospheric rivers linked to these waves. Similar patterns over the North Atlantic exhibiting a persistent zonally extended jet stream have been found to support cyclone clustering over western Europe (e.g., Pinto et al. 2014; Priestley et al. 2017b)

In the blocking patterns (Figs. 18c,d), anticyclonic wave breaking occurs on the downstream flank of a stationary blocking ridge, resulting in the formation of upper-level troughs and establishing and maintaining baroclinicity near the coast of North America. This configuration promotes repeated development and landfall of cyclones and atmospheric rivers along the U.S. coast. For the HPEs involving blocking over the Bering Sea–Alaska region (C4; Fig. 18d), as illustrated in the February 1986 case study, landfalling cyclones tend to propagate across the eastern North Pacific equatorward of the block into the region of anticyclonic wave breaking in conjunction with successive cyclonically breaking waves (i.e., negatively tilted PV streamers) extending from the upstream flank of the block. This blocking scenario closely resembles scenarios previously found to favor landfalling atmospheric rivers (e.g., Benedict et al. 2019) and HPEs (e.g., Carrera et al. 2004; Moore et al. 2020) along the West Coast.

The results of this study have elucidated key aspects of long-duration HPEs in Northern California; however, some aspects were not directly addressed and are left for future work. For instance, processes governing the formation and persistence of the large-scale patterns associated with the HPEs were not explicitly investigated. It is conceivable that eddy feedbacks (e.g., Shutts 1983; Rivière and Orlanski 2007) and Rossby wave forcing by tropical convection (e.g., Sardeshmukh and Hoskins 1988) play important roles in this respect. In addition, dynamical mechanisms that may contribute to cyclone clustering during the events were not diagnosed in detail. While successive upper-level Rossby waves appear to play a key role in the clustering, it is likely that secondary cyclogenesis driven by frontal instabilities and other mechanisms is also important in some cases.

The utility of the four HPE-related patterns for detecting HPEs in Northern California was explored through analysis of sets of close analogs for the patterns. For each pattern type, the likelihood of HPEs, especially those with a long duration, is significantly increased relative to random chance over Northern California and other parts of the West Coast region when an analog occurs. Additionally, composite analyses revealed key factors distinguishing analogs that result in a long-duration HPE from "ordinary" or null analogs that do not. Despite featuring similar large-scale conditions, the HPE and null analog cases exhibit critical differences in the structure and position of key flow features over the eastern North Pacific such that significantly higher cyclone frequencies and stronger IVT occur along the West Coast in the HPE cases.

The results of the analog-based analysis could provide a basis for applications in climate research and weather forecasting. For instance, the HPE-related patterns could be applicable for detecting HPEs in coarse-resolution general circulation model simulations, which tend to poorly represent precipitation in regions of complex terrain. Additionally, identification of the patterns in numerical model forecasts could provide increased situational awareness regarding the potential for heavy precipitation along the West Coast. This increased awareness is particularly relevant for late medium-range lead times (e.g., >10 days), at which models have limited skill in predicting precipitation over the West Coast (Pan et al. 2019), but may have some skill in predicting persistent large-scale flow patterns (e.g., Ferranti et al. 2018). Future research using model reforecasts could evaluate forecast skill for the HPE-related flow patterns and determine implications for precipitation forecasting.

Data availability statement. The UPD data were obtained from a NOAA/PSL archive at https://psl.noaa.gov/data/gridded/data.unified.html (Higgins et al. 2000; NOAA/NCEP/CPC 2020). The ERA-Interim data were obtained from the NCAR CISL Research Data Archive at https://doi.org/10.5065/D64747WN (ECMWF 2009; Dee et al. 2011). The ETOPO1 terrain elevation data were obtained from NOAA/NCEI at http://dx.doi.org/10.7289/V5C8276M (Amante and Eakins 2009; NOAA/NCEI 2020).

REFERENCES

Amante, C., and B. W. Eakins, 2009: ETOPO1 1-arc-minute global relief model: Procedures, data sources, and analysis. NOAA Tech. Memo. NESDIS NGDC-24, NOAA/National Geophysical Data Center, accessed 11 August 2020, https://doi.org/10.7289/V5C8276M.

Athanasiadis, P. J., J. M. Wallace, and J. J. Wettstein, 2010: Patterns of wintertime jet stream variability and their relation to the storm tracks. *J. Atmos. Sci.*, **67**, 1361–1381, https://doi.org/10.1175/2009JAS3270.1.

Barton, Y., P. Giannakaki, H. von Waldow, C. Chevalier, S. Pfahl, and O. Martius, 2016: Clustering of regional-scale extreme precipitation events in southern Switzerland. *Mon. Wea. Rev.*, **144**, 347–369, https://doi.org/10.1175/MWR-D-15-0205.1.

Benedict, J. J., A. C. Clement, and B. Medeiros, 2019: Atmospheric blocking and other large-scale precursor patterns of landfalling atmospheric rivers in the North Pacific: A CESM2 study. *J. Geophys. Res. Atmos.*, **124**, 11 330–11 353, https://doi.org/10.1029/2019JD030790.

Bezdek, J. C., R. Ehrlich, and W. Full, 1984: FCM: The fuzzy *c*-means clustering algorithm. *Comput. Geosci.*, **10**, 191–203, https://doi.org/10.1016/0098-3004(84)90020-7.

Bjerknes, J., and H. Solberg, 1922: Life cycle of cyclones and the polar front theory of atmospheric circulation. *Geofys. Publ.*, **3**, 3–18, https://doi.org/10.1002/qj.49704920609.

Carrera, M. L., R. W. Higgins, and V. E. Kousky, 2004: Downstream weather impacts associated with atmospheric blocking over the Northeast Pacific. *J. Climate*, **17**, 4823–4839, https://doi.org/10.1175/JCLI-3237.1.

Chen, M., W. Shi, P. Xie, V. B. S. Silva, V. E. Kousky, R. Wayne Higgins, and J. E. Janowiak, 2008: Assessing objective techniques for gauge-based analyses of global daily precipitation. *J. Geophys. Res.*, **113**, 1147, https://doi.org/10.1029/2007JD009132.

Cordeira, J. M., F. M. Ralph, and B. J. Moore, 2013: The development and evolution of two atmospheric rivers in proximity to western North Pacific tropical cyclones in October 2010. *Mon. Wea. Rev.*, **141**, 4234–4255, https://doi.org/10.1175/MWR-D-13-00019.1.

Dacre, H. F., and S. L. Gray, 2006: Life-cycle simulations of shallow frontal waves and the impact of deformation strain. *Quart. J. Roy. Meteor. Soc.*, **132**, 2171–2190, https://doi.org/10.1256/qj.05.238.

Dee, D. P., and Coauthors, 2011: The ERA-Interim reanalysis: Configuration and performance of the data assimilation system. *Quart. J. Roy. Meteor. Soc.*, **137**, 553–597, https://doi.org/10.1002/qj.828.

Dettinger, M. D., F. M. Ralph, T. Das, P. J. Neiman, and D. R. Cayan, 2011: Atmospheric rivers, floods and the water resources of California. *Water*, **3**, 445–478, https://doi.org/10.3390/w3020445.

Dole, R. M., 1986: Persistent anomalies of the extratropical Northern Hemisphere wintertime circulation: Structure. *Mon. Wea. Rev.*, **114**, 178–207, https://doi.org/10.1175/1520-0493(1986)114<0178:PAOTEN>2.0.CO;2.

Doswell, C. A., C. Ramis, R. Romero, and S. Alonso, 1998: A diagnostic study of three heavy precipitation episodes in the western Mediterranean region. *Wea. Forecasting*, **13**, 102–124, https://doi.org/10.1175/1520-0434(1998)013<0102: ADSOTH>2.0.CO;2.

ECMWF, 2009: ERA-Interim Project (updated monthly). NCAR Computational and Information Systems Laboratory Research Data Archive. Accessed 12 December 2019, https://doi.org/10.5065/D6CR5RD9.

Ensor, L. A., and S. M. Robeson, 2008: Statistical characteristics of daily precipitation: Comparisons of gridded and point datasets. *J. Appl. Meteor. Climatol.*, **47**, 2468–2476, https://doi.org/10.1175/2008JAMC1757.1.

Ferranti, L., L. Magnusson, F. Vitart, and D. S. Richardson, 2018: How far in advance can we predict changes in large-scale flow leading to severe cold conditions over Europe? *Quart. J. Roy. Meteor. Soc.*, **144**, 1788–1802, https://doi.org/10.1002/qj.3341.

Fish, M. A., A. M. Wilson, and F. M. Ralph, 2019: Atmospheric river families: Definition and associated synoptic conditions. *J. Hydrometeor.*, **20**, 2091–2108, https://doi.org/10.1175/JHM-D-18-0217.1.

Gochis, D., and Coauthors, 2015: The great Colorado flood of September 2013. *Bull. Amer. Meteor. Soc.*, **96**, 1461–1487, https://doi.org/10.1175/BAMS-D-13-00241.1.

Grams, C. M., H. Binder, S. Pfahl, N. Piaget, and H. Wernli, 2014: Atmospheric processes triggering the central European floods in June 2013. *Nat. Hazards Earth Syst. Sci.*, **14**, 1691–1702, https://doi.org/10.5194/nhess-14-1691-2014.

Guirguis, K., A. Gershunov, T. Shulgina, R. E. S. Clemesha, and F. M. Ralph, 2019: Atmospheric rivers impacting Northern California and their modulation by a variable climate. *Climate Dyn.*, **52**, 6569–6583, https://doi.org/10.1007/s00382-018-4532-5.

Higgins, R. W., W. Shi, E. Yarosh, and R. Joyce, 2000: *Improved United States Precipitation Quality Control System and Analysis*. NCEP/Climate Prediction Center Atlas 7, 40 pp.

Hoskins, B. J., I. Draghici, and H. C. Davies, 1978: A new look at the ω-equation. *Quart. J. Roy. Meteor. Soc.*, **104**, 31–38, https://doi.org/10.1002/qj.49710443903.

Joly, A., and A. J. Thorpe, 1990: Frontal instability generated by tropospheric potential vorticity anomalies. *Quart. J. Roy. Meteor. Soc.*, **116**, 525–560, https://doi.org/10.1002/qj.49711649302.

Keller, J. H., S. C. Jones, J. L. Evans, and P. A. Harr, 2011: Characteristics of the TIGGE multimodel ensemble prediction system in representing forecast variability associated with extratropical transition. *Geophys. Res. Lett.*, **38**, L12802, https://doi.org/10.1029/2011GL047275.

Kossin, J. P., 2018: A global slowdown of tropical-cyclone translation speed. *Nature*, **558**, 104–107, https://doi.org/10.1038/s41586-018-0158-3.

Lackmann, G. M., and J. R. Gyakum, 1999: Heavy cold-season precipitation in the northwestern United States: Synoptic climatology and an analysis of the flood of 17–18 January 1986. *Wea. Forecasting*, **14**, 687–700, https://doi.org/10.1175/1520-0434(1999)014<0687:HCSPIT>2.0.CO;2.

Lau, N.-C., 1988: Variability of the observed midlatitude storm tracks in relation to low-frequency changes in the circulation pattern. *J. Atmos. Sci.*, **45**, 2718–2743, https://doi.org/10.1175/1520-0469(1988)045<2718:VOTOMS>2.0.CO;2.

Lavers, D. A., and G. Villarini, 2013: The nexus between atmospheric rivers and extreme precipitation across Europe. *Geophys. Res. Lett.*, **40**, 3259–3264, https://doi.org/10.1002/grl.50636.

Lenggenhager, S., M. Croci-Maspoli, S. Brönnimann, and O. Martius, 2019: On the dynamical coupling between atmospheric blocks and heavy precipitation events: A discussion of the southern Alpine flood in October 2000. *Quart. J. Roy. Meteor. Soc.*, **60**, 1053, https://doi.org/10.1002/qj.3449.

Lindzen, R. S., and B. Farrell, 1980: A simple approximate result for the maximum growth rate of baroclinic instabilities. *J. Atmos. Sci.*, **37**, 1648–1654, https://doi.org/10.1175/1520-0469(1980)037<1648:ASARFT>2.0.CO;2.

Madonna, E., C. Li, C. M. Grams, and T. Woollings, 2017: The link between eddy-driven jet variability and weather regimes in the North Atlantic-European sector. *Quart. J. Roy. Meteor. Soc.*, **143**, 2960–2972, https://doi.org/10.1002/qj.3155.

Mailier, P. J., D. B. Stephenson, C. A. T. Ferro, and K. I. Hodges, 2006: Serial clustering of extratropical cyclones. *Mon. Wea. Rev.*, **134**, 2224–2240, https://doi.org/10.1175/MWR3160.1.

Martius, O., C. Schwierz, and H. C. Davies, 2010: Tropopause-level waveguides. *J. Atmos. Sci.*, **67**, 866–879, https://doi.org/10.1175/2009JAS2995.1.

——, and Coauthors, 2013: The role of upper-level dynamics and surface processes for the Pakistan flood of July 2010. *Quart. J. Roy. Meteor. Soc.*, **139**, 1780–1797, https://doi.org/10.1002/qj.2082.

McIntyre, M. E., and T. N. Palmer, 1983: Breaking planetary waves in the stratosphere. *Nature*, **305**, 593–600, https://doi.org/10.1038/305593a0.

Michelangeli, P.-A., R. Vautard, and B. Legras, 1995: Weather regimes: Recurrence and quasi-stationarity. *J. Atmos. Sci.*, **52**, 1237–1256, https://doi.org/10.1175/1520-0469(1995)052<1237:WRRAQS>2.0.CO;2.

Mo, K. C., and R. W. Higgins, 1998: Tropical convection and precipitation regimes in the western United States. *J. Climate*, **11**, 2404–2423, https://doi.org/10.1175/1520-0442(1998)011<2404:TCAPRI>2.0.CO;2.

Moore, B. J., D. Keyser, and L. F. Bosart, 2019: Linkages between extreme precipitation events in the central and eastern United States and Rossby wave breaking. *Mon. Wea. Rev.*, **147**, 3327–3349, https://doi.org/10.1175/MWR-D-19-0047.1.

——, A. B. White, D. J. Gottas, and P. J. Neiman, 2020: Extreme precipitation events in Northern California during winter 2016–17: Multiscale analysis and climatological perspective. *Mon. Wea. Rev.*, **148**, 1049–1074, https://doi.org/10.1175/MWR-D-19-0242.1.

Morgan, M. C., and J. W. Nielsen-Gammon, 1998: Using tropopause maps to diagnose midlatitude weather systems. *Mon. Wea. Rev.*, **126**, 2555–2579, https://doi.org/10.1175/1520-0493(1998)126<2555:UTMTDM>2.0.CO;2.

Mullen, S. L., 1987: Transient eddy forcing of blocking flows. *J. Atmos. Sci.*, **44**, 3–22, https://doi.org/10.1175/1520-0469(1987)044<0003:TEFOBF>2.0.CO;2.

Mundhenk, B. D., E. A. Barnes, E. D. Maloney, and K. M. Nardi, 2016: Modulation of atmospheric rivers near Alaska and the U.S. West Coast by northeast Pacific height anomalies. *J. Geophys. Res. Atmos.*, **121**, 12 751–12 765, https://doi.org/10.1002/2016JD025350.

Nakamura, H., and J. M. Wallace, 1990: Observed changes in baroclinic wave activity during the life cycles of low-frequency circulation anomalies. *J. Atmos. Sci.*, **47**, 1100–1116, https://doi.org/10.1175/1520-0469(1990)047<1100:OCIBWA>2.0.CO;2.

——, M. Nakamura, and J. L. Anderson, 1997: The role of high- and low-frequency dynamics in blocking formation. *Mon. Wea. Rev.*, **125**, 2074–2093, https://doi.org/10.1175/1520-0493(1997)125<2074:TROHAL>2.0.CO;2.

Nakamura, N., and C. S. Y. Huang, 2018: Atmospheric blocking as a traffic jam in the jet stream. *Science*, **361**, 42–47, https://doi.org/10.1126/science.aat0721.

Neiman, P. J., F. M. Ralph, G. A. Wick, J. D. Lundquist, and M. D. Dettinger, 2008: Meteorological characteristics and overland precipitation impacts of atmospheric rivers affecting the West Coast of North America based on eight years of SSM/I satellite observations. *J. Hydrometeor.*, **9**, 22–47, https://doi.org/10.1175/2007JHM855.1.

——, B. J. Moore, A. B. White, G. A. Wick, J. Aikins, D. L. Jackson, J. R. Spackman, and F. M. Ralph, 2016: An airborne and ground-based study of a long-lived and intense atmospheric river with mesoscale frontal waves impacting California during CalWater-2014. *Mon. Wea. Rev.*, **144**, 1115–1144, https://doi.org/10.1175/MWR-D-15-0319.1.

Newell, R. E., N. E. Newell, Y. Zhu, and C. Scott, 1992: Tropospheric rivers?—A pilot study. *Geophys. Res. Lett.*, **19**, 2401–2404, https://doi.org/10.1029/92GL02916.

NOAA/NCEI, 2020: ETOPO1 1-Arc-Minute Global Relief Model. NOAA National Centers for Environmental Information. Accessed 11 August 2020, https://doi.org/10.7289/V5C8276M.

NOAA/NCEP/CPC, 2020: Daily U.S. Unified Precipitation Dataset (updated daily). NOAA/OAR/ESRL/PSD Gridded Climate Dataset Archive. Accessed 12 December 2019, https://www.esrl.noaa.gov/psd/data/gridded/data.unified.html.

NOAA/NWS/CNRFC, 1986: Storm Summaries: Heavy precipitation event, California and Nevada, February 11–20, 1986. Accessed 1 October 2020, https://www.cnrfc.noaa.gov/storm_summaries/feb1986storms.php.

Pan, B., K. Hsu, A. AghaKouchak, S. Sorooshian, and W. Higgins, 2019: Precipitation prediction skill for the West Coast United States: From short to extended range. *J. Climate*, **32**, 161–182, https://doi.org/10.1175/JCLI-D-18-0355.1.

Pasquier, J. T., S. Pfahl, and C. M. Grams, 2019: Modulation of atmospheric river occurrence and associated precipitation extremes in the North Atlantic region by European weather regimes. *Geophys. Res. Lett.*, **46**, 1014–1023, https://doi.org/10.1029/2018GL081194.

Pfahl, S., and H. Wernli, 2012: Quantifying the relevance of cyclones for precipitation extremes. *J. Climate*, **25**, 6770–6780, https://doi.org/10.1175/JCLI-D-11-00705.1.

Pinto, J. G., I. Gómara, G. Masato, H. F. Dacre, T. Woollings, and R. Caballero, 2014: Large-scale dynamics associated with clustering of extratropical cyclones affecting Western Europe. *J. Geophys. Res. Atmos.*, **119**, 13 704–13 719, https://doi.org/10.1002/2014JD022305.

Press, W. H., S. A. Teukolsky, W. T. Vetterling, and B. P. Flannery, 2007: Numerical Recipes: The Art of Scientific Computing. 3rd ed. Cambridge University Press, 1235 pp.

Priestley, M. D. K., J. G. Pinto, H. F. Dacre, and L. C. Shaffrey, 2017a: The role of cyclone clustering during the stormy winter of 2013/2014. *Weather*, **72**, 187–192, https://doi.org/10.1002/wea.3025.

——, ——, ——, and ——, 2017b: Rossby wave breaking, the upper-level jet, and serial clustering of extratropical cyclones in Western Europe. *Geophys. Res. Lett.*, **44**, 514–521, https://doi.org/10.1002/2016GL071277.

——, H. F. Dacre, L. C. Shaffrey, S. Schemm, and J. G. Pinto, 2020: The role of secondary cyclones and cyclone families for the North Atlantic storm track and clustering over Western Europe. *Quart. J. Roy. Meteor. Soc.*, **146**, 1184–1205, https://doi.org/10.1002/qj.3733.

Quiroz, R. S., 1983: The climate of the "El Niño" winter of 1982–83—A season of extraordinary climatic anomalies. *Mon. Wea. Rev.*, **111**, 1685–1706, https://doi.org/10.1175/1520-0493(1983)111<1685:TCOTNW>2.0.CO;2.

Ralph, F. M., P. J. Neiman, and G. A. Wick, 2004: Satellite and CALJET aircraft observations of atmospheric rivers over the eastern North Pacific Ocean during the winter of 1997/98. *Mon. Wea. Rev.*, **132**, 1721–1745, https://doi.org/10.1175/1520-0493(2004)132<1721:SACAOO>2.0.CO;2.

——, ——, ——, S. I. Gutman, M. D. Dettinger, D. R. Cayan, and A. B. White, 2006: Flooding on California's Russian River: Role of atmospheric rivers. *Geophys. Res. Lett.*, **33**, L13801, https://doi.org/10.1029/2006GL026689.

——, ——, G. N. Kiladis, K. Weickmann, and D. W. Reynolds, 2011: A multiscale observational case study of a Pacific atmospheric river exhibiting tropical–extratropical connections and a mesoscale frontal wave. *Mon. Wea. Rev.*, **139**, 1169–1189, https://doi.org/10.1175/2010MWR3596.1.

——, T. Coleman, P. J. Neiman, R. J. Zamora, and M. D. Dettinger, 2013: Observed impacts of duration and seasonality of atmospheric-river landfalls on soil moisture and runoff in coastal Northern California. *J. Hydrometeor.*, **14**, 443–459, https://doi.org/10.1175/JHM-D-12-076.1.

——, M. D. Dettinger, M. M. Cairns, T. J. Galarneau, and J. Eylander, 2018: Defining "Atmospheric River": How the *Glossary of Meteorology* helped resolve a debate. *Bull. Amer. Meteor. Soc.*, **99**, 837–839, https://doi.org/10.1175/BAMS-D-17-0157.1.

——, J. J. Rutz, J. M. Cordeira, M. Dettinger, M. Anderson, D. Reynolds, L. J. Schick, and C. Smallcomb, 2019: A scale to characterize the strength and impacts of atmospheric rivers. *Bull. Amer. Meteor. Soc.*, **100**, 269–289, https://doi.org/10.1175/BAMS-D-18-0023.1.

Reinhold, B. B., and R. T. Pierrehumbert, 1982: Dynamics of weather regimes: Quasi-stationary waves and blocking. *Mon. Wea. Rev.*, **110**, 1105–1145, https://doi.org/10.1175/1520-0493(1982)110<1105:DOWRQS>2.0.CO;2.

Rex, D. F., 1950: Blocking action in the middle troposphere and its effect upon regional climate. *Tellus*, **2**, 196–211, https://doi.org/10.3402/tellusa.v2i3.8546.

Risser, M. D., and M. F. Wehner, 2017: Attributable human-induced changes in the likelihood and magnitude of the observed extreme precipitation during Hurricane Harvey. *Geophys. Res. Lett.*, **44**, 12 457–12 464, https://doi.org/10.1002/2017GL075888.

Rivière, G., and I. Orlanski, 2007: Characteristics of the Atlantic storm-track eddy activity and its relation with the North Atlantic Oscillation. *J. Atmos. Sci.*, **64**, 241–266, https://doi.org/10.1175/JAS3850.1.

Robertson, A. W., and M. Ghil, 1999: Large-scale weather regimes and local climate over the western United States. *J. Climate*, **12**, 1796–1813, https://doi.org/10.1175/1520-0442(1999)012<1796:LSWRAL>2.0.CO;2.

Röthlisberger, M., L. Frossard, L. F. Bosart, D. Keyser, and O. Martius, 2019: Recurrent synoptic-scale Rossby wave patterns and their effect on the persistence of cold and hot spells. *J. Climate*, **32**, 3207–3226, https://doi.org/10.1175/JCLI-D-18-0664.1.

Ryoo, J.-M., Y. Kaspi, D. W. Waugh, G. N. Kiladis, D. E. Waliser, E. J. Fetzer, and J. Kim, 2013: Impact of Rossby wave breaking on U.S. West Coast winter precipitation during ENSO events.

J. Climate, **26**, 6360–6382, https://doi.org/10.1175/JCLI-D-12-00297.1.

Sardeshmukh, P. D., and B. J. Hoskins, 1988: The generation of global rotational flow by steady idealized tropical divergence. *J. Atmos. Sci.*, **45**, 1228–1251, https://doi.org/10.1175/1520-0469(1988)045<1228:TGOGRF>2.0.CO;2.

Schär, C., and H. C. Davies, 1990: An instability of mature cold fronts. *J. Atmos. Sci.*, **47**, 929–950, https://doi.org/10.1175/1520-0469(1990)047<0929:AIOMCF>2.0.CO;2.

Schemm, S., and M. Sprenger, 2015: Frontal-wave cyclogenesis in the North Atlantic— A climatological characterisation. *Quart. J. Roy. Meteor. Soc.*, **141**, 2989–3005, https://doi.org/10.1002/qj.2584.

Schwierz, C., M. Croci-Maspoli, and H. C. Davies, 2004: Perspicacious indicators of atmospheric blocking. *Geophys. Res. Lett.*, **31**, L06125, https://doi.org/10.1029/2003GL019341.

Shutts, G. J., 1983: The propagation of eddies in diffluent jet-streams: Eddy vorticity forcing of "blocking" flow fields. *Quart. J. Roy. Meteor. Soc.*, **109**, 737–761, https://doi.org/10.1002/qj.49710946204.

Sodemann, H., and A. Stohl, 2013: Moisture origin and meridional transport in atmospheric rivers and their association with multiple cyclones. *Mon. Wea. Rev.*, **141**, 2850–2868, https://doi.org/10.1175/MWR-D-12-00256.1.

Thorncroft, C. D., B. J. Hoskins, and M. E. Mcintyre, 1993: Two paradigms of baroclinic-wave life-cycle behaviour. *Quart. J. Roy. Meteor. Soc.*, **119**, 17–55, https://doi.org/10.1002/qj.49711950903.

Tuttle, J. D., and C. A. Davis, 2006: Corridors of warm season precipitation in the central United States. *Mon. Wea. Rev.*, **134**, 2297–2317, https://doi.org/10.1175/MWR3188.1.

USGS, 1995: Northern California storms and floods of January 1995. Fact Sheet 062-95, 2 pp., https://doi.org/10.3133/fs06295.

Wallace, J. M., G.-H. Lim, and M. L. Blackmon, 1988: Relationship between cyclone tracks, anticyclone tracks and baroclinic waveguides. *J. Atmos. Sci.*, **45**, 439–462, https://doi.org/10.1175/1520-0469(1988)045<0439:RBCTAT>2.0.CO;2.

Weaver, R. L., 1962: Meteorology of Hydrologically Critical Storms in California. U.S. Department of Commerce, Weather Bureau, 207 pp.

Weijenborg, C., and T. Spengler, 2020: Diabatic heating as a pathway for cyclone clustering encompassing the extreme storm Dagmar. *Geophys. Res. Lett.*, **47**, e2019GL085777, https://doi.org/10.1029/2019GL085777.

Wernli, H., and C. Schwierz, 2006: Surface cyclones in the ERA-40 dataset (1958–2001). Part I: Novel identification method and global climatology. *J. Atmos. Sci.*, **63**, 2486–2507, https://doi.org/10.1175/JAS3766.1.

——, and M. Sprenger, 2007: Identification and ERA-15 climatology of potential vorticity streamers and cutoffs near the extratropical tropopause. *J. Atmos. Sci.*, **64**, 1569–1586, https://doi.org/10.1175/JAS3912.1.

——, S. Pfahl, J. Trentmann, and M. Zimmer, 2010: How representative were the meteorological conditions during the COPS field experiment in summer 2007? *Meteor. Z.*, **19**, 619–630, https://doi.org/10.1127/0941-2948/2010/0483.

White, A. B., B. J. Moore, D. J. Gottas, and P. J. Neiman, 2019: Winter storm conditions leading to excessive runoff above California's Oroville Dam during January and February 2017. *Bull. Amer. Meteor. Soc.*, **100**, 55–70, https://doi.org/10.1175/BAMS-D-18-0091.1.

Wilks, D. S., 2011: *Statistical Methods in the Atmospheric Sciences*. 3rd ed. International Geophysics Series, Vol. 100, Academic Press, 704 pp.

Winters, A. C., D. Keyser, and L. F. Bosart, 2019: The development of the North Pacific jet phase diagram as an objective tool to monitor the state and forecast skill of the upper-tropospheric flow pattern. *Wea. Forecasting*, **34**, 199–219, https://doi.org/10.1175/WAF-D-18-0106.1.

Zhu, Y., and R. E. Newell, 1998: A proposed algorithm for moisture fluxes from atmospheric rivers. *Mon. Wea. Rev.*, **126**, 725–735, https://doi.org/10.1175/1520-0493(1998)126<0725:APAFMF>2.0.CO;2.